RSC Advances

REVIEW

View Article Online
View Journal | View Issue

Open Access Article. Published on 28 July 2025. Downloaded on 12/27/2025 3:34:44 PM.
This article is licensed under a Creative Commons Attribution-NonCommercial 3.0 Unported Licence.

Check for updates

Cite this: *RSC Adv.*, 2025, **15**, 26919

Recent progress in graphene-based materials for thermoelectric applications

Xingyu Xue, Songjun Li and Maiyong Zhu *

Received 21st May 2025
Accepted 22nd July 2025

DOI: 10.1039/d5ra03577e

rsc.li/rsc-advances

Graphene, with its outstanding electrical conductivity, low thermal conductivity, tunable nanostructure, mechanical flexibility, chemical stability, two-dimensional structure, and large specific surface area, exhibits significant potential in thermoelectric materials. These unique properties make graphene a promising candidate for thermoelectric applications. This paper will discuss the latest research achievements and summaries of graphene in the thermoelectric field from three perspectives: pristine graphene, graphene-inorganic composites, and graphene-organic composites. The goal of this review is to enhance the selection and design of graphene based materials and the development of thermoelectric fields.

1 Introduction

Entering the 21st century, the sense of urgency regarding energy has intensified, leading to a greater appreciation for the development and utilization of existing energy resources. The thermoelectric effect, discovered in the early 19th century, is now receiving increasing attention from researchers due to the growing demand for waste heat recovery and advancements in research technologies.[1] Graphene, first prepared and discovered by British scientists in the early 21st century, has also become a focal point of study.[2] The thermoelectric performance of a material is typically evaluated using the dimensional figure of merit "Thermoelectric Figure of Merit" (ZT), while the performance of a thermoelectric converter is assessed using another dimensionless figure of merit, the "Power Factor" (PF).[3] Both ZT and PF are positively correlated with the material's Seebeck coefficient (S) and electrical conductivity (σ). Additionally, ZT is positively correlated with the material's temperature (T) and negatively correlated with its thermal conductivity (κ). The dimensionless thermoelectric figure of merit (ZT) is given by the following eqn (1):[4]

$$ZT = \frac{S^2\sigma T}{\kappa} = \frac{S^2\sigma T}{(\kappa_e + \kappa_l)} \tag{1}$$

where (κ_l) is the lattice thermal conductivity and (κ_e) is the electronic thermal conductivity.[5] The power factor is given by the eqn (2):

$$\mathrm{PF} = S^2\sigma \tag{2}$$

Graphene, with its outstanding electrical conductivity, low thermal conductivity, tunable nanostructure, mechanical flexibility, chemical stability, two-dimensional structure, and large specific surface area, exhibits significant potential in thermoelectric materials.[6,7] These properties have made graphene a good carrier, which is widely used in the research of biological detection, food safety[8] and even agriculture.[9] These properties also make graphene a great potential in thermoelectric materials. Numerous scholars have conducted research and compiled findings on the aforementioned aspects. For instance, Tabitha A. Amollo *et al.*[5] have provided a detailed exposition on the factors influencing the thermoelectric properties of graphene, focusing on its electrical and thermal characteristics. Similarly, Rafiq Mulla *et al.*[6] have summarized the thermoelectric performance of graphene in composites with both organic and inorganic materials.

In recent years, due to the relatively low thermoelectric conversion efficiency (generally below 8%) of current thermoelectric materials, their applications have been largely limited to sensor technologies. These materials exhibit high sensitivity to temperature variations and can directly convert thermal signals into electrical signals, making them ideal for fire alarm systems[10] and a critical component in IoT (Internet of Things) applications.[11] In building construction, thermoelectric materials serve multiple functions, including temperature monitoring, building cooling, and even energy harvesting.[12] Additionally, leveraging the exceptional flexibility of certain organic thermoelectric materials, researchers have developed wearable thermoelectric devices tailored to human motion.[13] These devices can capture physiological signals generated by the body, enabling applications in medical diagnostics. The research on graphene has been developed rapidly either, especially in the field of thermoelectricity. Breakfasts were made almost every four years (as shown in Fig. 1): the graphene morphology separated from the original few layers of graphene to graphene nanoband, graphene quantum dots;[14,15]

School of Materials Science & Engineering, Jiangsu University, Zhenjiang, 212013, China. E-mail: maiyongzhu@ujs.edu.cn

© 2025 The Author(s). Published by the Royal Society of Chemistry

Open Access Article. Published on 28 July 2025. Downloaded on 12/27/2025 3:34:44 PM.
This article is licensed under a Creative Commons Attribution-NonCommercial 3.0 Unported Licence.

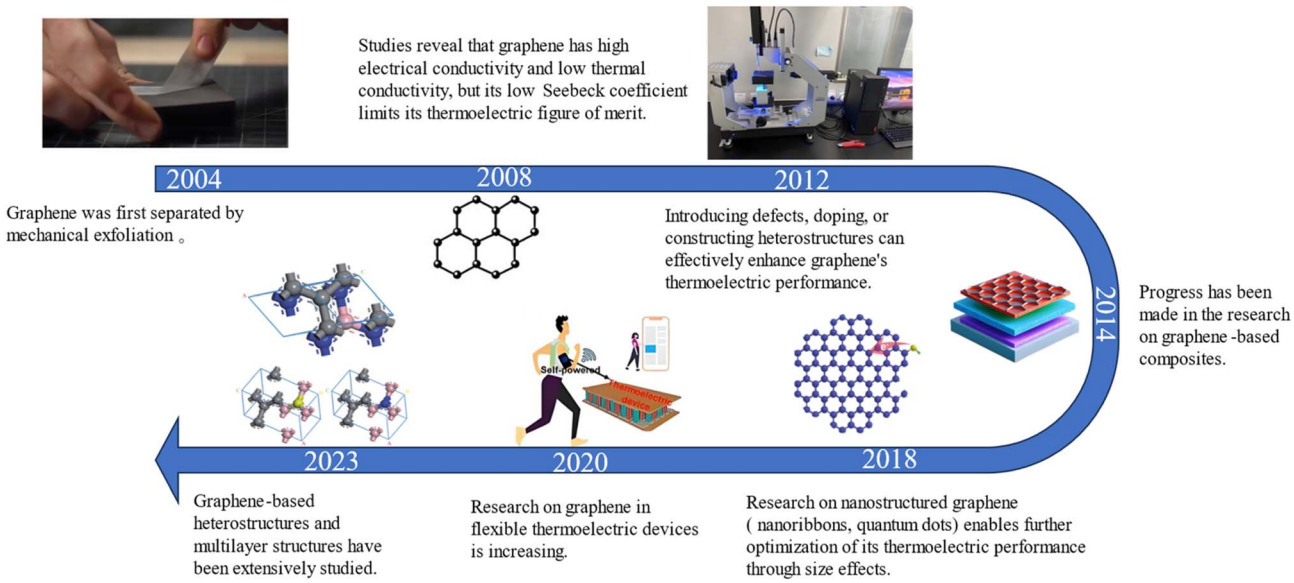

Fig. 1 Timeline of advances in graphene for thermoelectric applications. Reproduced from ref. 23 and 24 with permission. Copyright 2022 the Acta Materiae Compositae Sinica, Reproduced from ref. 25 with permission. Copyright 2022 Wiley-VCH.

modification of graphene from simple oxidation–reduction[16] to complex defect engineering, surface modification;[17] compound graphene from inorganic material to organic material; applications for graphene thermoelectric materials range[18] from simple energy converters to health monitoring tools[19] that are adaptable to humans.[20,21]

Looking ahead, what directions will the development of graphene-based thermoelectric materials take? Which factors will be pivotal in enhancing the thermoelectric performance of graphene? These are questions that the scientific community is eager to answer. This paper will explore the latest research achievements in the field of graphene thermoelectrics, examining three key areas: graphene itself, graphene-inorganic composites, and graphene-organic composites. Following the general logic and sequence of scientific inquiry, from simple to complex modifications of graphene, this article aims to dissect the underlying principles governing the variations in graphene's thermoelectric properties.[22]

2 Pristine graphene

Graphene has numerous applications in the thermoelectric field, some of which involve the direct use of graphene or modified graphene. Among these, modified graphene plays a predominant role. The following sections will detail the direct applications of graphene and modified graphene.[5,26]

2.1 Physical modification of graphene

Physical modification of graphene primarily involves altering its physical structure through physical means to influence its thermoelectric properties.[27] Currently, the graphene available on the market is mostly graphene nanosheets (composed of multiple layers of graphene stacked together, typically fewer than 10 layers, with a thickness ranging from 1 to 10 nanometers). These nanosheets account for over 80% of the total graphene market sales.[28] Compared to single-layer graphene, graphene nanosheets exhibit higher mechanical strength and lower production costs, making them the primary focus of physical modification.[29]

Zaferani and colleagues[30] investigated the thermoelectric properties of graphene nanosheets and noted that, due to their multi-layer stacked structure, graphene nanosheets are generally considered two-dimensional materials. However, compared to single-layer graphene, they contain grains whose size is influenced by the preparation process. Graphene nanosheets are prone to various lattice defects, which are detrimental to carrier transport,[31] resulting in lower electrical conductivity compared to single-layer graphene. But these defects at crystal boundaries also increase phonon scattering and achieve lattice softening in inorganic thermoelectric materials,[32] providing conditions for reducing the material's thermal conductivity.[33]

Saqib Rafique[34] and colleagues developed a novel dry physical rolling synthesis method. They compressed raw materials into small pellets and then sintered them under high temperature and pressure to synthesize new few-layer graphene nanosheet-based particles, with an average layer count of 4–5 layers (as Fig. 2a and b). Thermoelectric performance measurements revealed anisotropic performance parameters in the horizontal and vertical pressure directions. Fig. 2c shows that the electrical conductivity changes almost linearly in the vertical and horizontal pressure directions (Fig. 2c–h shows the thermoelectric properties of a few layer graphene (FLG) nanosheet), but the conductivity in the direction parallel to the pressure is significantly lower than in the vertical direction. This is due to the grain boundaries formed between graphene nanosheets in the parallel direction, which affect electron transport. Similarly, Fig. 2f shows that the thermal conductivity in the parallel direction is significantly lower than in the vertical direction due to fewer grain

 © 2025 The Author(s). Published by the Royal Society of Chemistry

Open Access Article. Published on 28 July 2025. Downloaded on 12/27/2025 3:34:44 PM.
This article is licensed under a Creative Commons Attribution-NonCommercial 3.0 Unported Licence.

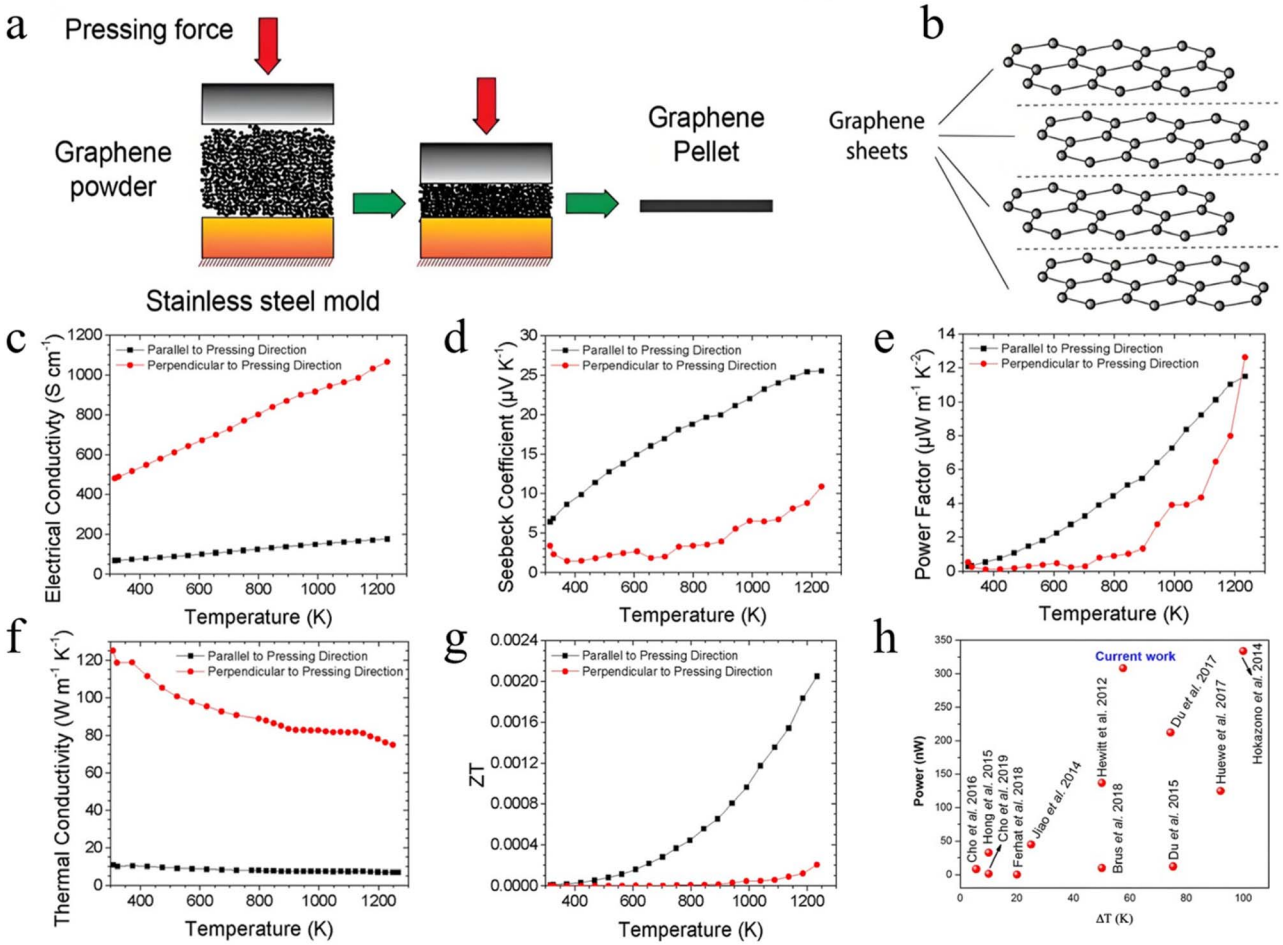

Fig. 2 (a) Schematic of the pellet making process from FLG powder, (b) molecular structures of the FLG nanoflakes. Thermoelectric properties of the FLG nanoflake-based pellets. (c) Electrical conductivity, (d) Seebeck coefficient, (e) power factor (f) thermal conductivity, and (g) figure of merit, parallel to and perpendicular to the pressing directions. (h) Comparison of the results of the article. Reproduced from ref. 34 with permission. Copyright 2020 the American Chemical Society.

boundaries in the parallel direction, which cause both electron and phonon scattering. This fully demonstrates the characteristics of graphene materials and the controllability of the synthesis process to a certain extent.

In practical applications, Zhang and colleagues[35] used graphene nanosheets and polydimethylsiloxane (PDMS) to create a wearable, highly elastic graphene thermoelectric sponge. This sponge exhibits a high Seebeck coefficient of 49.2 μV K^{-1} at room temperature and a large compressive strain of 98%. After 10 000 compression cycles at 30% strain, the experiment attributed its performance to favorable interfacial interactions between graphene sheets and PDMS precursor molecular chains. The sponge demonstrated excellent mechanical and thermoelectric stability, generating enough electricity to power low-power medical devices for monitoring physiological signals.

2.2 Chemical modification of graphene

Chemical modification of graphene primarily involves altering its physical structure and semiconductor type through chemical means. The targets of chemical modification are typically few-layer graphene, graphene oxide, reduced graphene oxide, and graphene quantum dots. Common chemical treatments for graphene include oxidation methods such as Hummers' method,[36] Brodie's method,[37] and electrochemical methods[38] to prepare graphene oxide (GO). Reduced graphene oxide (rGO) can be prepared by heating in a hydrogen flow or treating with hydrazine hydrate solution. Hyunwoo and colleagues[39] found that the temperature during the reduction of graphene oxide affects the thermoelectric properties of the resulting reduced graphene oxide. Controlling the reduction temperature can improve the Seebeck coefficient of reduced graphene oxide.

Constructing thermoelectric generators requires n-type and p-type semiconductor thermoelectric materials to form p–n junctions.[40] Pure graphene is a zero-bandgap semiconductor, with its conduction and valence bands touching at the Dirac point, resulting in no bandgap.[41] To change the semiconductor type of graphene for better adaptation in thermoelectric devices, special organic solutions can be used.[42] For example, treating graphene with polyethyleneimine can convert it into an n-type semiconductor, while treating it with polyacrylic acid can

Open Access Article. Published on 28 July 2025. Downloaded on 12/27/2025 3:34:44 PM.
This article is licensed under a Creative Commons Attribution-NonCommercial 3.0 Unported Licence.

convert it into a p-type semiconductor.[43,44] Novak[45] and colleagues demonstrated that changing the adsorbed surfactants during the intercalation–exfoliation step in the solution-phase exfoliation method can also alter the semiconductor type of graphene. Polyvinylpyrrolidone (PVP) surfactant results in n-type graphene, while pyrenebutyric acid (PBA) surfactant results in p-type graphene. Experimental measurements showed that the modified n-type and p-type graphene films have high thermoelectric windows. Compared to organic conductive polymers like PEDOT:PSS, PBA and PVP do not decompose until nearly 300 °C. The thermoelectric devices constructed from these graphene films achieved extremely high electrical conductivity (3010 and 2330 S cm^{-1}) and high Seebeck coefficients (53.1 and −45.5 μV K^{-1}), with a power factor exceeding 600 μW $m^{-1}K^{-2}$ at room temperature.

Chemical vapor deposition (CVD) is another high-quality, large-area, and controllable method for preparing graphene.[46–48] Its advantage lies in its ability to produce large-area graphene with uniform thickness and fewer defects, while also allowing for controlled modification of graphene.[49] Myungwoo Choi and colleagues[50] introduced a method for synthesizing high-performance graphene *via* Atomic-Scale Defect Engineering using Mobile Hot-Wire Chemical Vapor Deposition Systems (MHW-CVD). The specific procedure involves using a molybdenum substrate and tungsten wire in an MHW-CVD furnace. The Cu foil is loaded into the chamber under vacuum, and the substrate and tungsten wire are heated under a H_2 flow with the total pressure regulated by a throttle valve. A CH_4/H_2 mixed gas is then injected into the chamber until the entire Cu foil is scanned by the heated wire. After scanning, the system is rapidly cooled to room temperature under a H_2 flow. Fig. 3a shows this preparation process, Fig. 3b–g compares the thermoelectric properties of graphene prepared by MHW-CVD with graphene prepared by conventional chemical vapor deposition (C-CVD) and Fig. 3h–k are Selected Area Electron Diffraction (SAED) diagrams. Due to the nanoscale roughness of the Cu foil surface, the high-angle tilt boundary domains formed by the tungsten wire scanning at controlled speeds create charge carrier energy filtering potential barriers, reducing charge carrier concentration and effectively increasing the Seebeck coefficient. This significantly enhances the thermoelectric performance of graphene. At 350 K, the *ZT* value of this graphene was calculated to be 3.78×10^{-3}, seven times that of conventional CVD graphene (5.42×10^{-4}) and the highest value for single-layer CVD graphene films.

In practical applications, traditional 2D graphene faces challenges in composite materials due to its structural characteristics, such as agglomeration and uneven distribution, making it difficult to combine well with other materials without complex composite processes.[47] CVD-prepared graphene exhibits excellent thermoelectric performance due to its unique three-dimensional structure with multiple angles and voids, resembling bulk materials.[51] This allows it to be combined with almost any porous material through simple cold rolling

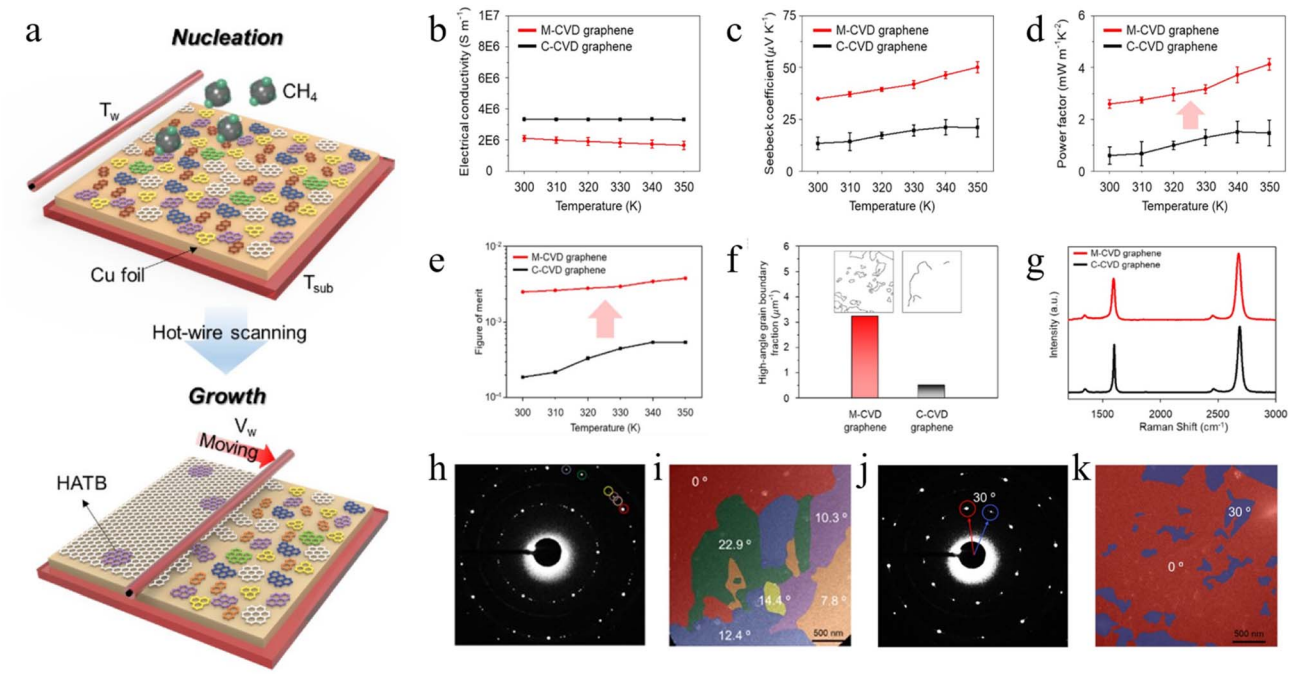

Fig. 3 (a) Graphene growth mechanism in the MHW-CVD system. (b) Electrical conductivity, (c) Seebeck coefficient, (d) power factor of the M-CVD graphene and C-CVD graphene as a function of temperature. (e) Comparison of the *ZT* values of the M-CVD graphene and C-CVD graphene as a function of temperature. (f) High-angle grain boundary fraction of the M-CVD graphene and C-CVD graphene. (g) Raman spectrum of the M-CVD graphene and C-CVD graphene. (h) SAED pattern of the as-grown graphene *via* the MHW-CVD system. (i) False-colored DF-TEM image of an as-grown graphene corresponding to the SAED pattern in (h). (j) SAED pattern of the as-grown graphene *via* the conventional CVD system. (k) False-colored DF-TEM image of an as-grown graphene corresponding with SAED pattern in (j). Reproduced from ref. 50 with permission. Copyright 2021 the American Chemical Society.

 © 2025 The Author(s). Published by the Royal Society of Chemistry

Open Access Article. Published on 28 July 2025. Downloaded on 12/27/2025 3:34:44 PM.
This article is licensed under a Creative Commons Attribution-NonCommercial 3.0 Unported Licence.

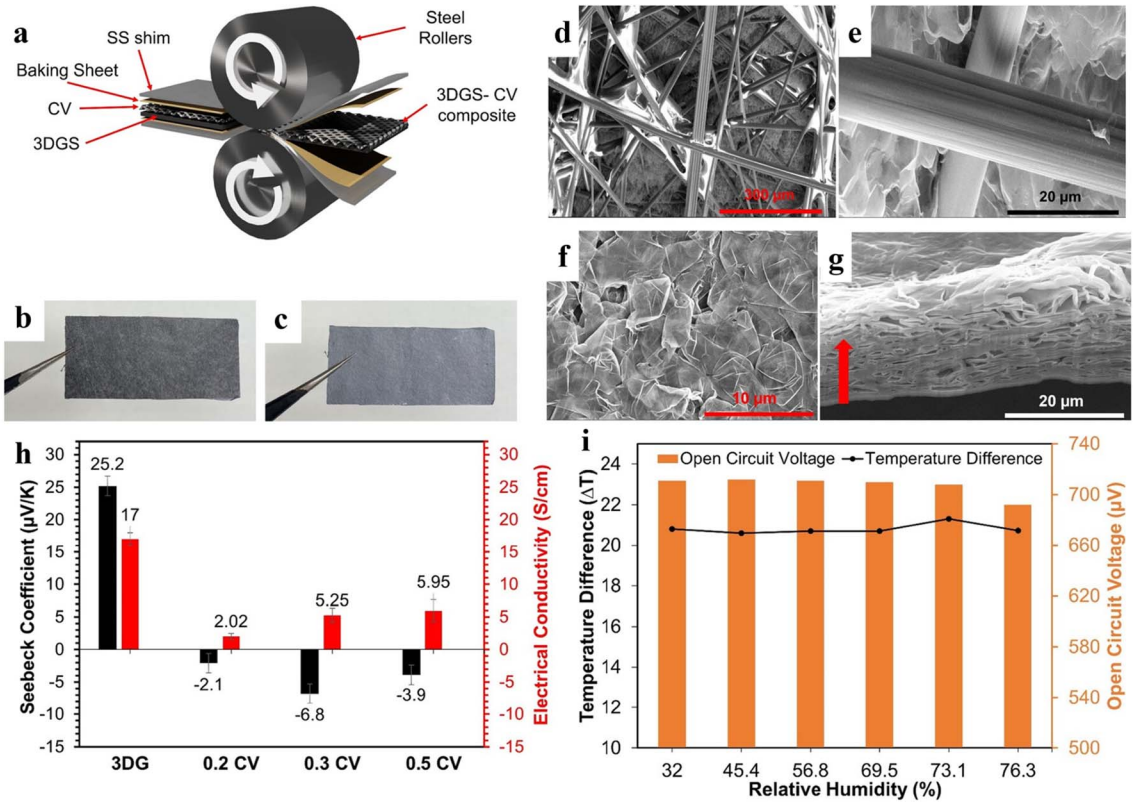

Fig. 4 (a) Diagram of cold rolling process synthesis for 3DGS-CV composite materials; (b) CV surface of composite materials; and the 3DGS surface of (c) composite material. (d) SEM image of the CV surface of 3DGS-CV composite material. (e) SEM image of the interface between graphite fibers and 3DGS. (f) SEM image of composite material 3DGS surface. (g) FIB cutting cross-section of 3DGS-CV composite material. The red arrow points in the direction of extrusion. (h) The conductivity and Seebeck coefficient of 3DGS and various densities of 0.2 g cm^{-3} (0.2CV), 0.3 g cm^{-3} (0.3CV), and 0.5 g cm^{-3} (0.5CV) CV. (i) The effect of relative humidity (RH) at room temperature on the thermoelectric voltage and ΔT of 3DGS-CV composite materials. Reproduced from ref. 52 with permission. Copyright 2024 the American Chemical Society.

processes. Kondapalli and colleagues[52] found that CVD-prepared graphene not only performs well in thermoelectric applications but also forms a three-dimensional structure with multiple angles and voids, similar to bulk materials. In their study, they combined CVD-prepared three-dimensional graphene (3DGS) with commercially available carbon veil (CV) through cold rolling to form a 3DGS-CV composite thermoelectric material (as Fig. 4a). This composite material has two sides: one carbon veil side and one three-dimensional graphene side (as Fig. 4b and c), inherently containing both p–n junctions. By stacking two 3DGS-CV composite thermoelectric materials with different sides together, a thermoelectric converter can be constructed. Fig. 4d–f are SEM plots of 3DGS-CV composite thermoelectric materials, and Fig. 4h and i are thermoelectric properties. This film-based device can function not only as a thermoelectric converter but also as a photoelectric converter due to its sensitivity to light.

3 Graphene/inorganic composite

Among thermoelectric materials, inorganic thermoelectric material heat is considered the most promising to break through $ZT = 3$ in a laboratory environment. The conventional approach to enhancing the thermoelectric performance of inorganic materials involves doping with metalloid elements (*e.g.*, tellurium, Te) and rare-earth elements (*e.g.*, lanthanum, La). This strategy primarily works by: (1) increasing charge carrier concentration through elemental doping; (2) reducing lattice thermal conductivity (κ_l) *via* defect engineering.[53] However, most of these dopants are not only prohibitively expensive but also non-renewable, which significantly hinders their large-scale commercial application in thermoelectric devices. This limitation has driven the urgent need to explore alternative materials and approaches for performance optimization.

As a material with excellent electrical and thermal properties, graphene is often used as an "additive" in most cases to be added with corresponding materials to improve or enhance its original special properties.[54] Among many materials composite with graphene, the composite of graphene and inorganic materials accounts for a large proportion, especially inorganic non-metallic materials. Graphene can well improve their electrical properties and change the internal structure of the material. Composition of graphene with inorganic materials will be introduced later in the article from the four aspects shown in Fig. 5.

Open Access Article. Published on 28 July 2025. Downloaded on 12/27/2025 3:34:44 PM.
This article is licensed under a Creative Commons Attribution-NonCommercial 3.0 Unported Licence.

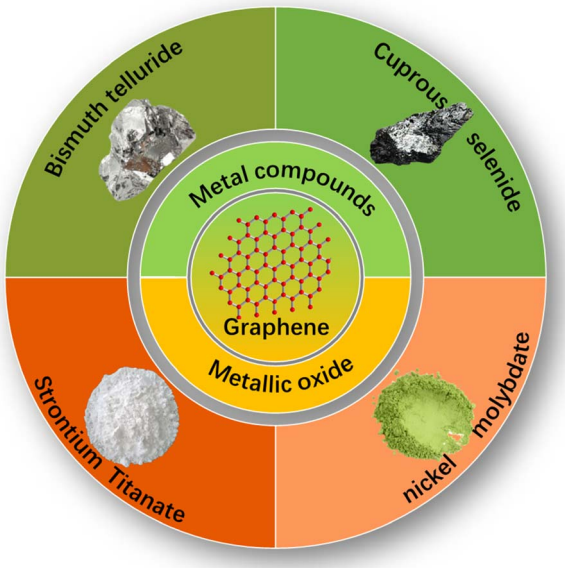

Fig. 5 Graphene mixed with different types of inorganic materials.

3.1 Composite with Bi_2Te_3

In the research on various thermoelectric materials, bismuth telluride is one of the thermoelectric materials with excellent thermoelectric properties at room temperature.[55] Due to its good electrical conductivity and low thermal conductivity, extensive research has been conducted on the thermoelectric properties of bismuth telluride.[56] However, the excellent thermoelectric conversion efficiency of bismuth telluride still remains strong in the face of people's demand for thermoelectric conversion, which is also the reason why although it has excellent thermoelectric performance, it is difficult to obtain large-scale commercial applications.[57] People have proposed many methods and made many attempts to improve the thermoelectric properties of bismuth telluride.[58]

Dresselhaus and his colleagues proposed a solution to improve the power factor of thermoelectric materials by reducing their dimensionality. Kaleem Ahmad *et al.*[59] reported a method to improve the thermoelectric properties of bismuth telluride by adding graphene with different volume fraction contents to bismuth telluride. According to reports, the experiment involved preparing an ethanol dispersion of ground graphene and bismuth telluride, ultrasonically mixing them in different volume fractions, and high-temperature sintering to obtain experimental graphene doped bismuth telluride samples. By observing the Scanning Electron Microscopy (SEM) images of bismuth telluride samples with different volume fractions of graphene doping shown in Fig. 6a and b, we can observe that as the graphene content increases, the surface of bismuth telluride flakes is more coated with graphene nanoparticles and the smoothness decreases. Through experimental measurements of the thermoelectric properties of the samples (as shown in Fig. 6c–h), we can see that the doping of graphene has an enhancing effect on parameters that are beneficial for improving thermoelectric performance, while it has a suppressing effect on the decrease in thermal conductivity. This may be due to two reasons: firstly, mechanical deformation of bismuth telluride particles occurs after ball milling, resulting in a donor like effect that increases the conductivity of the material. Secondly, the addition of graphene enhances the barrier scattering and percolation effects of composite materials, which mainly have a positive impact on the Seebeck coefficient and conductivity. Meanwhile, the addition of graphene suppresses the growth of bismuth telluride lattice, creating conditions for more phonon scattering interfaces and reducing lattice thermal conductivity. Ultimately, in terms of thermoelectric

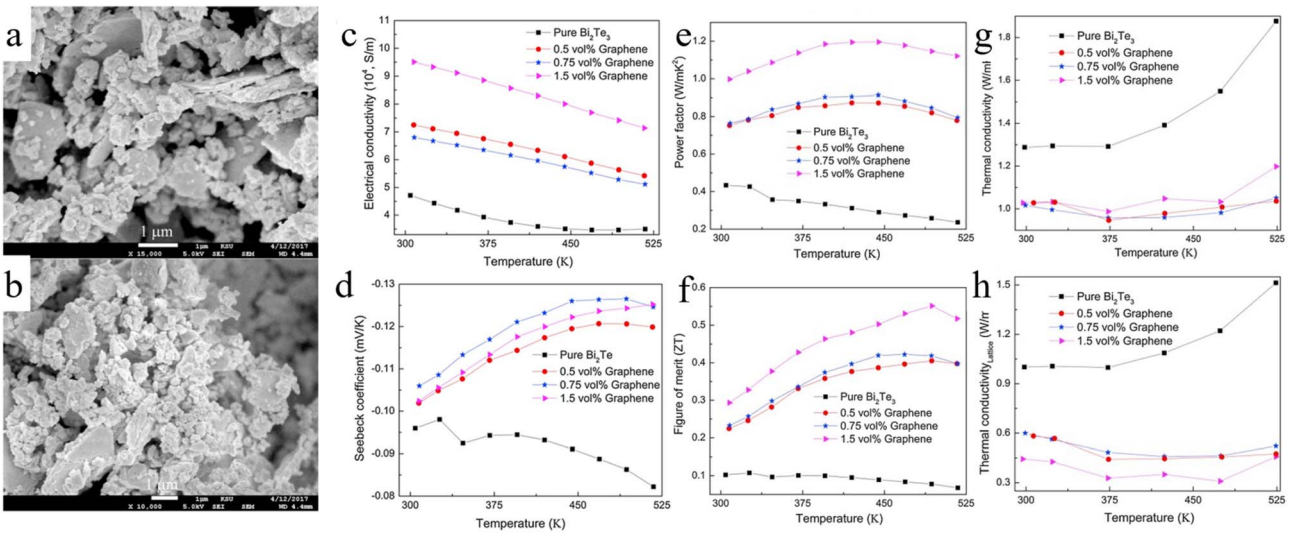

Fig. 6 SEM image of (a) 0.75 (b) 1.5, vol% graphene/Bi_2Te_3 composite powders; (c–h) represents the thermoelectric properties of samples doped with graphene at different volume fractions and temperatures, (c) conductivity, (d) Seebeck coefficient, (e) power factor, (f) *ZT* value, (g) thermal conductivity, (h) lattice thermal conductivity. Reproduced from ref. 59 with permission. Copyright 2019 the Elsevier.

 © 2025 The Author(s). Published by the Royal Society of Chemistry

Open Access Article. Published on 28 July 2025. Downloaded on 12/27/2025 3:34:44 PM.
This article is licensed under a Creative Commons Attribution-NonCommercial 3.0 Unported Licence.

performance, the addition of 1.5 vol% graphene resulted in the most beneficial thermoelectric performance.

In order to further investigate the role of graphene in modifying the thermoelectric properties of bismuth telluride, Shuankui Li *et al.*[60] reported a study using graphene quantum dots (GQDs) doped with bismuth telluride. They prepared two types of graphene quantum dot solutions (5 nm, 20 nm) in size (4 mg mL^{-1}) by filtration and dialysis using graphene oxide (GO). Then, add 1 ml, 2 ml, 3 ml, and 4 ml of graphene quantum dot solution to the bismuth telluride precursor solution. By adding vitamin C, an oxidation–reduction reaction occurs, resulting in the formation of bismuth telluride on the surface of graphene quantum dot nanosheets, forming Bi_2Te_3/GQDs hybrid nanosheets (as shown in Fig. 7a). After discharge plasma sintering, Bi_2Te_3/GQDs hybrid nanosheets suitable for performance testing were obtained. Through the thermoelectric performance testing of Bi_2Te_3/GQDs hybrid nanosheets, a sample thermoelectric performance variation curve as shown in the Fig. 7c–h was obtained. We can see from Fig. 7c that the addition of graphene quantum dots is detrimental to the conductivity of the sample, and generally, as the degree of graphene quantum dot addition increases, the conductivity decreases. This is because with the addition of graphene quantum dots, the interface density of the sample also increases, which hinders the migration of charge carriers in the thermoelectric material (as shown in Fig. 7b), ultimately reducing the overall conductivity of the sample. However, the addition of graphene quantum dots also increases the conductivity of the sample at higher temperatures compared to pure bismuth telluride, which may be due to the increased concentration of charge carriers (graphene quantum dots synthesized from oxidized graphene provide O vacancies). From Fig. 7f and g, it can be seen that the addition of graphene quantum dots significantly reduces the electronic thermal conductivity and lattice thermal conductivity, and the graphene quantum dots with larger average sizes (20 nm) have a better effect on reducing thermal conductivity than those with smaller sizes (5 nm). This may be due to the positive effect of graphene quantum addition on phonon scattering at the interface, where the interface area in Bi_2Te_3/GQD-20 nm is larger than that in Bi_2Te_3/GQD-5 nm. Finally, by measuring the thermoelectric figure of merit, it can be seen that the Bi_2Te_3/GQDs-20 nm hybrid nanosheet achieves a maximum *ZT* of 0.55 at 425 K, which is higher than the *ZT* of Bi_2Te_3 nanosheets without hybrid nanostructures. Graphene plays multiple roles as a nucleation center, impurity, and electron donor in Bi_2Te_3/GQD hybrid nanosheets, and has a complex impact on the electronic properties of Bi_2Te_3/GQD hybrid materials.

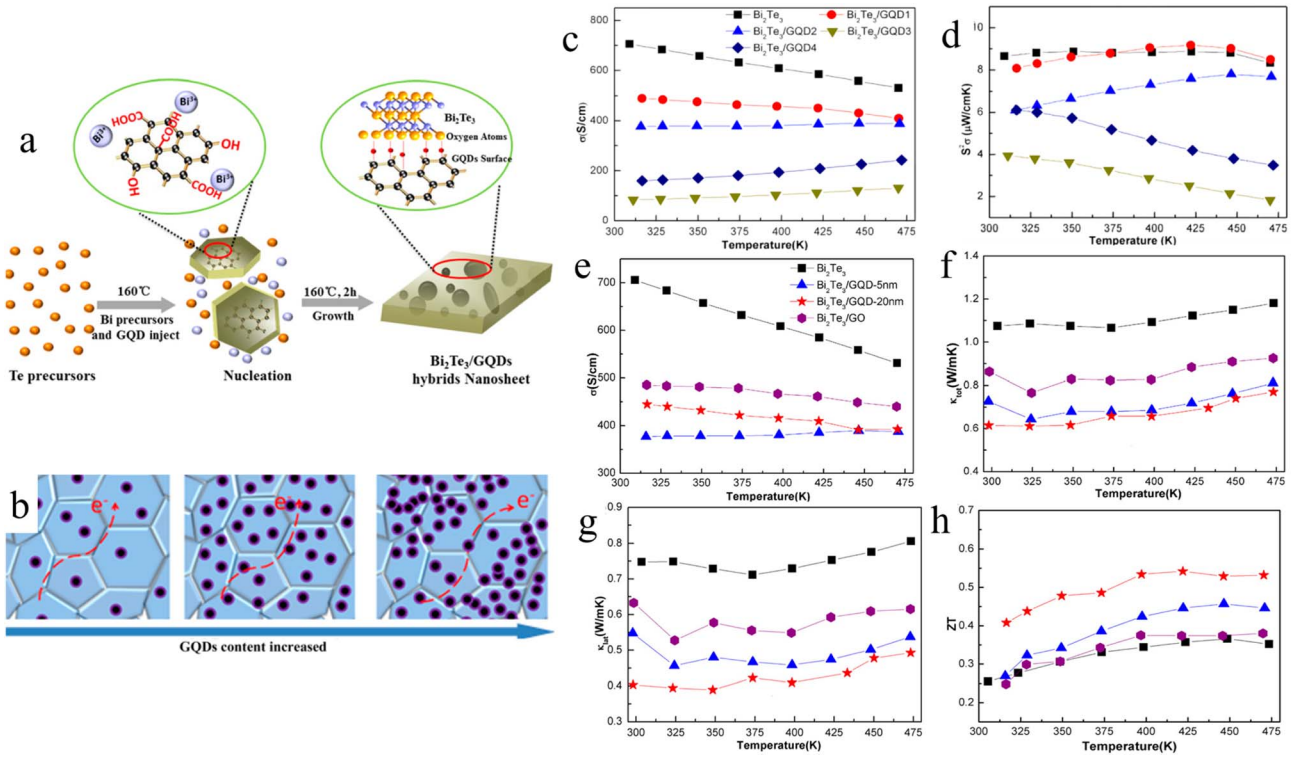

Fig. 7 (a) Schematic diagram of the synthesis of Bi_2Te_3/GQDs hybrid nanosheets. (b) Schematic diagram of electron transport pathways in Bi_2Te_3/GQD mixtures with different GQD contents. The thermal and electrical properties of Bi_2Te_3/GQDs with different GQD contents, represented as Bi_2Te_3/GQDs *x* (*x* is the volume of GQD solution (4 mg mL^{-1})), as a function of temperature are plotted as follows: (c) conductivity, (d) power factor. The thermoelectric properties of Bi_2Te_3/GQD hybrid synthesized using two sizes of GQD, GQD-5 nm (average size about 5 nm) and GQD-20 nm (average size about 20 nm), as well as graphene oxide (GO), as a function of temperature: (e) electrical conductivity, (f) electronic thermal conductivity, (g) lattice thermal conductivity, (h) thermoelectric figure of merit; all Bi_2Te_3/GQD hybrids have the same GQD content (2 mL GQD solution (4 mg mL^{-1})). Reproduced from ref. 60 with permission. Copyright 2017 the American Chemical Society.

Open Access Article. Published on 28 July 2025. Downloaded on 12/27/2025 3:34:44 PM.
This article is licensed under a Creative Commons Attribution-NonCommercial 3.0 Unported Licence.

As we know from the previous text, the doping of graphene has a special effect on the thermoelectric properties of bismuth telluride.[61] Afterwards, people are also searching for more forms of graphene and using more methods to add graphene for thermoelectric modification of bismuth telluride.[62] Jinhee Bae *et al.*[63] synthesized a novel thermoelectric material by incorporating edge oxide graphene (EOG) into Se free n-type $Bi_{1.7}Sb_{0.3}Te_3$ (BST) using 3D printing technology. The specific operation process is to add edge oxidized graphene to dimethylformamide, disperse it with glycerol, and then add it to antimony doped bismuth telluride dispersion as the ink for 3D printing. After printing, place the finished product into a sintering furnace for sintering without any external load, remove organic matter, and obtain EGO-BST samples that can be used for experimental testing (as Fig. 8a). After observing SEM images, it was found that with the increase of EOG content, the densification of the sample decreased significantly, and the grain growth was affected by EOG, resulting in a significant increase in voids. After conducting thermoelectric performance measurements, obtain the thermoelectric performance diagram of the sample (as Fig. 8b–g). It was found that the conductivity decreased significantly compared to pure BST after the content of edge graphene oxide was 0.2 wt% (as Fig. 8b). This may be due to the influence of the voids mentioned earlier on the propagation of charge carriers. After measurement, the carrier mobility decreased significantly after the content of edge graphene oxide was 0.2 wt%. However, measuring the carrier concentration revealed that the carrier concentration increased slightly after the graphene content reached 0.2 wt% (as Fig. 8e). At the same time, the thermal conductivity of the sample was also measured. With the addition of edge graphene, the proportion of phonon thermal conductivity gradually increased, which is closely related to the porous structure of the 3D printed sample (as Fig. 8h). The final experiment showed that at the optimal EOG content, 0.1 wt% EOG-BST exhibited a peak *ZT* value of 0.71, and the output power (0.32 μW) increased by 2 times compared to pure BST (as Fig. 8g). 3D printing provides the possibility for the commercial application of graphene doped thermoelectric materials.

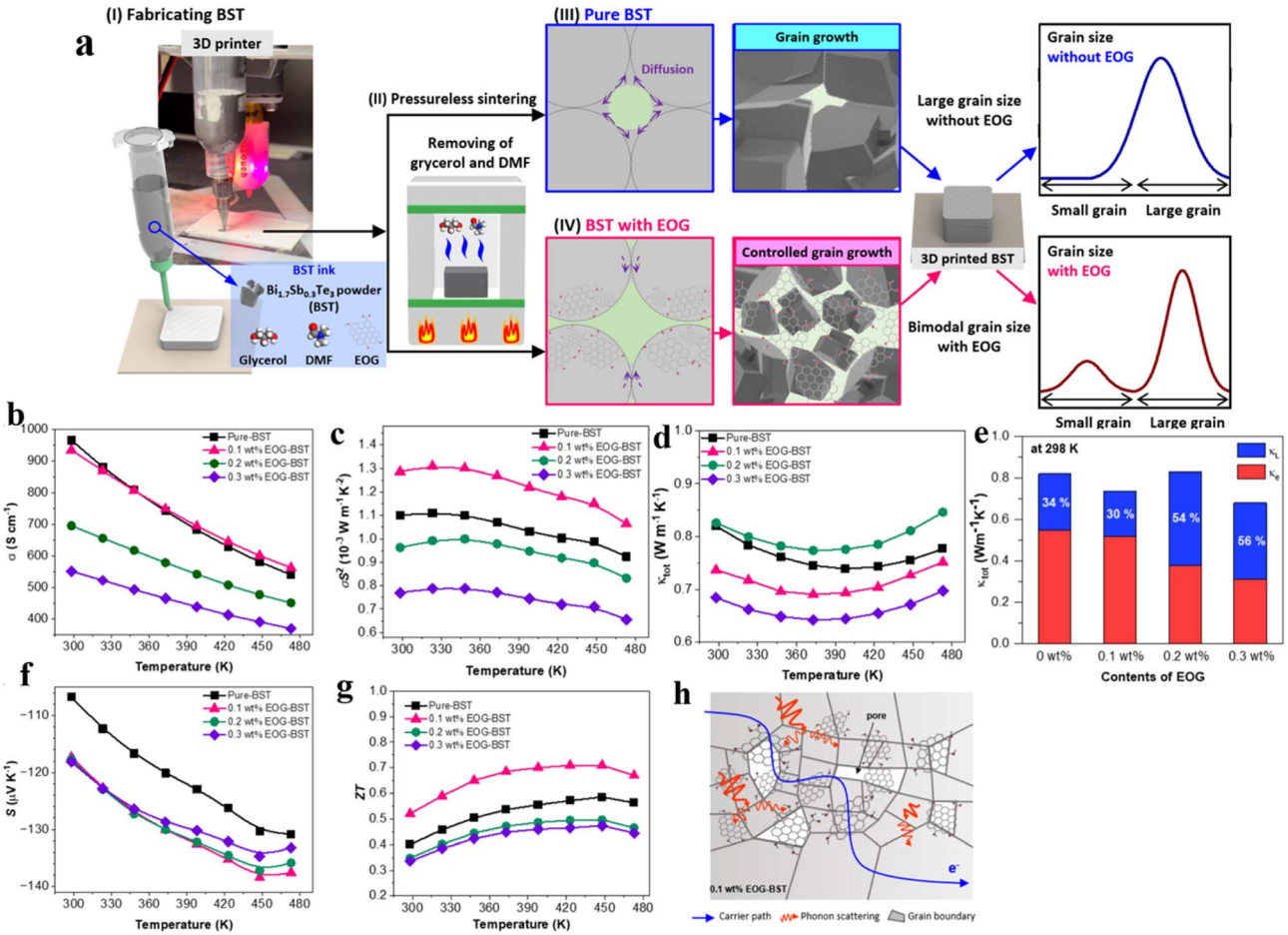

Fig. 8 (a) Schematic diagram of 3D printing preparation process for BST and EGO-BST. Thermoelectric performance changes of EGO-BST samples with different EGO contents with temperature: (b) conductivity; (c) power factor; (d) total thermal conductivity; (e) the ratio within the total thermal conductivity, electronic thermal conductivity k_e (red) and lattice thermal conductivity k_l (blue); (f) Seebeck coefficient; (g) thermoelectric optimal value. (h) Assumption diagram of electron paths and phonon scattering on 0.1 wt% EOG-BST sample. Reproduced from ref. 63 with permission. Copyright 2024 the American Chemical Society.

 © 2025 The Author(s). Published by the Royal Society of Chemistry

Open Access Article. Published on 28 July 2025. Downloaded on 12/27/2025 3:34:44 PM.
This article is licensed under a Creative Commons Attribution-NonCommercial 3.0 Unported Licence.

3.2 Composite with Cu_2Se

There are various types of thermoelectric materials, among which Cu_2Se is currently the focus of research in the field.[64,65] The advantage of Cu_2Se is that it has a good *ZT* value and is a typical fast ion conductor thermoelectric material.[66]

Meng Li *et al.*[67] reported the performance testing and analysis of graphene doped Cu_2Se. They thoroughly ground and mixed graphene nanosheets and Cu_2Se powder. Placed the mixed powder in a vacuum environment and heat it by shaking on an acetylene oxygen flame for 10 minutes. After the mixed powder is completely cooled and melted, it is rapidly cooled down in liquid nitrogen. Subsequently, the sample to be tested was annealed in an argon atmosphere at 600 °C. The formation of Cu_2Se small grains can be observed in the sample through STEM images. At the same time, carbon inclusions are located at the edge of grain boundaries. Through measurement, it was also found that there was significant lattice expansion in the Cu_2Se matrix plane (as shown in Fig. 9a and b). This may be due to the random movement of graphene nanosheets in molten Cu_2Se at a high temperature of 1200 °C which remained insoluble and form individual two-dimensional carbon nanosheets, or cluster together. After cooling, carbon inclusions of a certain size were formed at the lattice boundaries in the sample. The above phenomenon effectively suppresses the propagation of phonons in the sample material. It can be clearly seen from Fig. 9e that the addition of graphene reduces the thermal conductivity of the sample. Unfortunately, with the addition of graphene, the conductivity and power factor of the sample also decreased, which is detrimental to the improvement of the thermoelectric performance of the thermoelectric material (as shown in Fig. 9d and f). This may be due to a small amount of carbon dissolved in the liquid Cu_2Se, causing the lattice of Cu_2Se to alloy and the lattice of Cu_2Se to be damaged (Fig. 9b and c). Although the addition of graphene has advantages and disadvantages for different thermoelectric parameters of Cu_2Se, the final measure of a material's thermoelectric performance is its thermoelectric merit value-*ZT*. The final *ZT* value, as shown in Fig. 9g, shows an increasing trend with the addition of graphene, indicating that the beneficial effect of graphene on the thermal conductivity of Cu_2Se is greater than its adverse effect on electrical conductivity. Therefore, the final *ZT* value is the ultra-high thermoelectric figure of merit of $ZT = 2.44 \pm 0.25$ for carbon reinforced Cu_2Se at 870 K with a mass fraction of 0.15% graphene added.

With the deepening of research on Cu_2Se as a thermoelectric material, the hot spot advantages of Cu_2Se are gradually being discovered. The excellent thermoelectric performance of Cu_2Se is related to the high mobility of Cu^+ ions. At the same time, some drawbacks of Cu_2Se have gradually been exposed. Due to the need to convert thermal energy into electrical energy, thermoelectric materials often operate in high temperatures.[68] People have found that the thermoelectric performance of Cu_2Se decreases significantly in high-temperature environments.[69] The reason for this is that at high temperatures, molecular thermal motion intensifies, and the highly mobile Cu^+ ions on the crystal surface of Cu_2Se material, which are beneficial for improving thermoelectric performance, undergo superionization. Cu^+ ions escape from the original lattice and no longer reset, leading to a sharp decline in thermoelectric performance.[70]

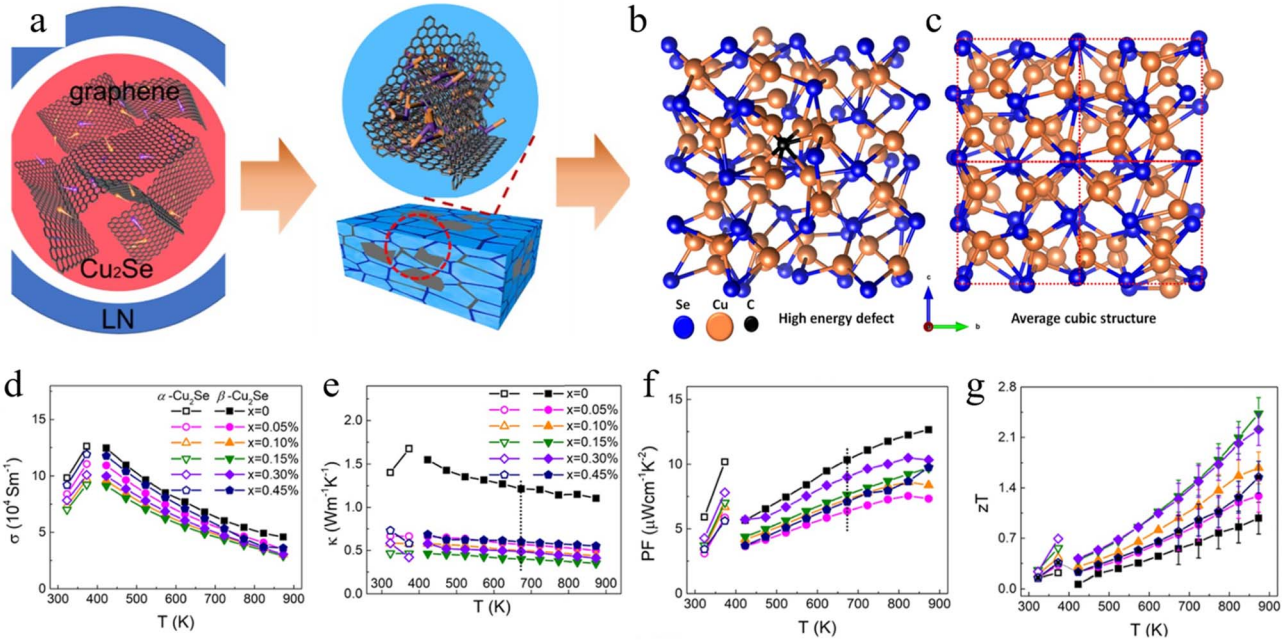

Fig. 9 (a) Schematic diagram of the nucleation process of small grains caused by graphene doping. (b) Calculate the Cu_2Se lattice theoretical configuration of interstitial carbon defects simulated using density functional theory. (c) Conventional Cu_2Se lattice theoretical configuration (d) thermal conductivity (e), electrical conductivity (f), power factor (g), thermoelectric figure of merit, (d–f), and (g) are all plotted as a function of temperature. Reproduced from ref. 67 with permission. Copyright 2018 the Elsevier.

Open Access Article. Published on 28 July 2025. Downloaded on 12/27/2025 3:34:44 PM.
This article is licensed under a Creative Commons Attribution-NonCommercial 3.0 Unported Licence.

For this reason, Zhou Zhifang and others[71] from the Tsinghua University team successfully improved the hot spot performance of Cu_2Se in the high temperature range while enhancing the original thermoelectric performance by introducing $Bi_{0.88}Pb_{0.06}Ca_{0.06}CuSeO$ (BPCCSO) and graphene doping. Their research is divided into two parts. Firstly, Cu_2Se BPCCSO thermoelectric composite material samples were prepared by mixing and sintering powders. Through experimental testing, it was found that the introduction of BPCCSO successfully established an ion barrier interface (as shown in Fig. 10a–c), effectively preventing the long-range migration of Cu^+ ions at high temperatures. This greatly improves the problem of thermoelectric loss in high temperature range of Cu_2Se based thermoelectric materials. However, it is precisely due to the introduction of BPCCSO that the electrical conductivity, power factor, and other thermoelectric parameters of Cu_2Se BPCCSO composite thermoelectric materials slightly decrease compared to Cu_2Se in the lower temperature range. This is still due to the obstruction of Cu^+ ion migration. In order to further improve the thermoelectric properties of Cu_2Se BPCCSO composite thermoelectric materials, the article proposes introducing graphene to fully grind and cold press the original Cu_2Se BPCCSO composite thermoelectric material into pellets. After adding graphene, it is fused using self propagating high-temperature synthesis (SHS), and finally, after thorough grinding, mixing, and discharge plasma sintering, Cu_2Se BPCCSO graphene composite thermoelectric material samples are obtained. Through experimental testing, the addition of graphene has improved a series of thermoelectric parameters and thermoelectric advantages, such as Seebeck coefficient (as shown in Fig. 10d), electrical conductivity (as shown in Fig. 10e), and thermal conductivity (as shown in Fig. 10g). The final ZT_{max} value at 1000 K is approximately 2.82473, and the ZT average value within the range of 1000 K is approximately 1.73 (as shown in Fig. 10h). The reason for this is due to the excellent conductivity of graphene, and the establishment of graphene conductive bands in the material increases the conductivity. The introduction of graphene adds another interface, causing phonons to undergo multiple scattering between multiple scattering sources (BPCCSO, Cu_2Se is also a scattering source) during propagation, thereby reducing thermal conductivity.

3.3 Composite with nickel molybdate

At present, materials with excellent thermoelectric properties discovered through research are concentrated on metals and metal compounds, such as Bi_2Te_3 and Cu_2Se.As mentioned earlier, people have raised higher requirements for the operating temperature of thermoelectric materials, especially for thermoelectric conversion in high-temperature environments. Traditional metals and metal compounds often decompose in the high temperature range, leading to a sharp decline in thermoelectric performance and making it difficult to perform thermoelectric converters under high temperature conditions.[72] So people turned their attention to metal oxides, which have stable chemical and physical properties under high temperature conditions,[73] and nickel molybdate (NMO) is one of them.

Nickel molybdate has excellent electrical and thermal properties and is widely used in supercapacitors and sensors.[74,75] The

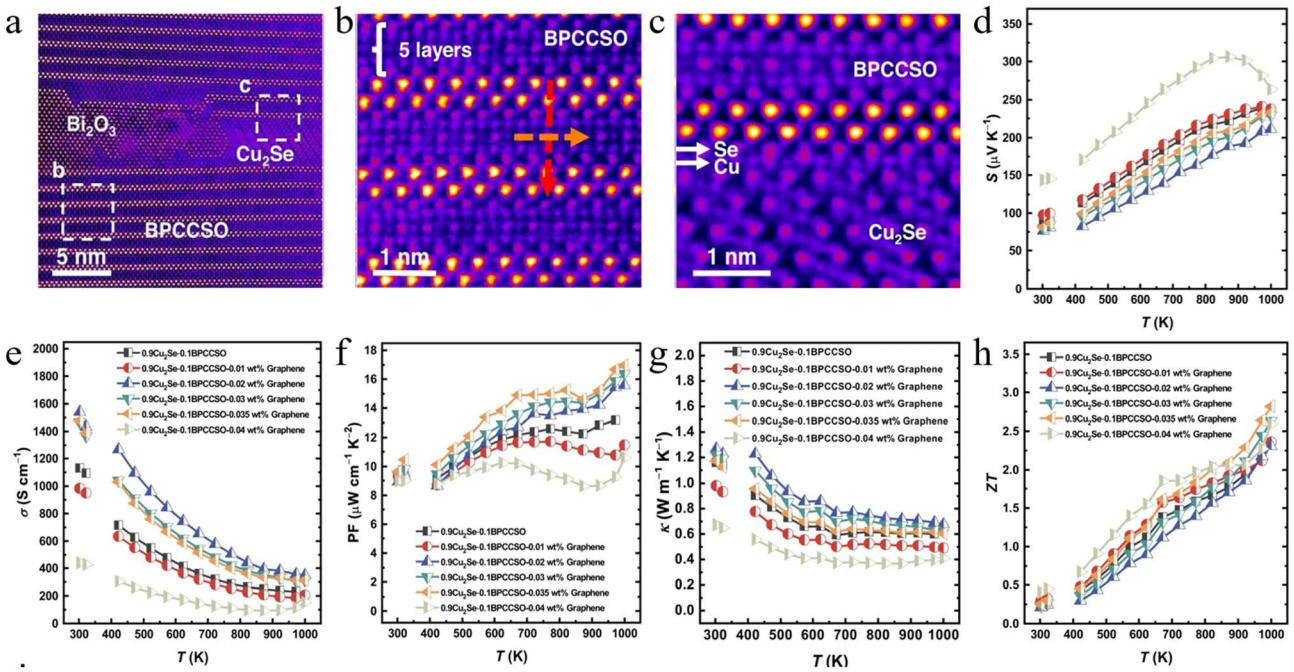

Fig. 10 (a) HAADF-STEM images of Cu_2Se BPCCSO composite thermoelectric material; (b and c) this is an enlarged image of region b and region c in (a). (d–h) Are the thermoelectric properties of Cu_2Se BPCCSO graphene composite thermoelectric materials with different graphene contents at different temperatures: (d) Seebeck coefficient, (e) conductivity, (f) power factor, (g) thermal conductivity, (h) thermoelectric figure of merit. Reproduced from ref. 71 with permission. Copyright 2023 published by Springer Nature under a CC-BY license.

 © 2025 The Author(s). Published by the Royal Society of Chemistry

Open Access Article. Published on 28 July 2025. Downloaded on 12/27/2025 3:34:44 PM.
This article is licensed under a Creative Commons Attribution-NonCommercial 3.0 Unported Licence.

addition of nickel can modulate the thermoelectric properties of molybdenum compounds.[76] Aishwarya *et al.*[77] studied the thermoelectric properties of nickel molybdate and prepared a nickel molybdate/graphene oxide (NMO/rGO) composite thermoelectric material with high thermoelectric properties by adding graphene oxide (rGO). According to reports, they prepared pure nickel molybdate samples using solvothermal synthesis method. Then, add graphene oxide to the sample, disperse it by ultrasound, and heat it in a high-pressure reactor (as shown in Fig. 11a). Finally, dry it to obtain NMO/rGO composite thermoelectric material (as shown in Fig. 11b and c). By comparing the performance parameters of the samples, it was found that after adding graphene oxide, the NMO/rGO composite thermoelectric material showed a significant improvement in all the thermoelectric performance parameters measured in the article, including conductivity, carrier mobility, Seebeck coefficient, power factor, and numerical values, compared to the original nickel molybdate. Especially the power factor, the value has increased by two orders of magnitude. The thermal conductivity (as shown in Fig. 11d and e) decreases, and the thermal conductivity changes little with temperature. The reason for this is that the addition of graphene oxide reduces the potential barrier between grain boundaries, lowers the activation energy required for charge carriers to cross grain boundaries, and constructs a two-dimensional conductive network between nickel molybdate nanorods (as shown in Fig. 11f). Meanwhile, due to the addition of graphene oxide, phonon scattering increases and thermal conductivity decreases. The type of semiconductor material has also changed. Sodium molybdate has transformed from n-type semiconductor electron conductivity to p-type semiconductor hole conductivity. This may be due to the vacancies of oxygen atoms provided by graphene oxide. Ultimately, the comparison of thermoelectric figures of merit confirms that nickel molybdate is uniquely suited for hybridization with reduced graphene oxide (as shown in Fig. 11g). The resulting NMO/rGO composite achieves an approximately 135-fold enhancement in *ZT* relative to pristine NMO (as shown in Fig. 11h and i).

3.4 Composite with $SrTiO_3$

La-mixed $SrTiO_3$ (LSTO) is a metal oxide thermoelectric material with high *ZT* value that has been studied much in recent decades. Among them, $SrTiO_3$ has a large carrier effective mass, good stability, thermal stability and a strong structural volume for replacing hybrids.[78] Therefore, $SrTiO_3$ can be mixed with trivalent elements (*e.g.*, La, Dy) or pentavalent elements (Nb) to reduce its thermal conductivity while maintaining its thermoelectric properties.[79,80] However, with the deepening of research, it is found that the thermoelectric performance of $SrTiO_3$ is difficult to improve, and its thermoelectric performance advantage is not obvious compared with traditional metal materials.

Conventional thermoelectric materials have a "thermal window" period.[81] Within this temperature range of this "thermal window" period, the thermoelectric properties of thermoelectric materials are remarkable, and they can effectively convert thermal energy into electrical energy. Outside of

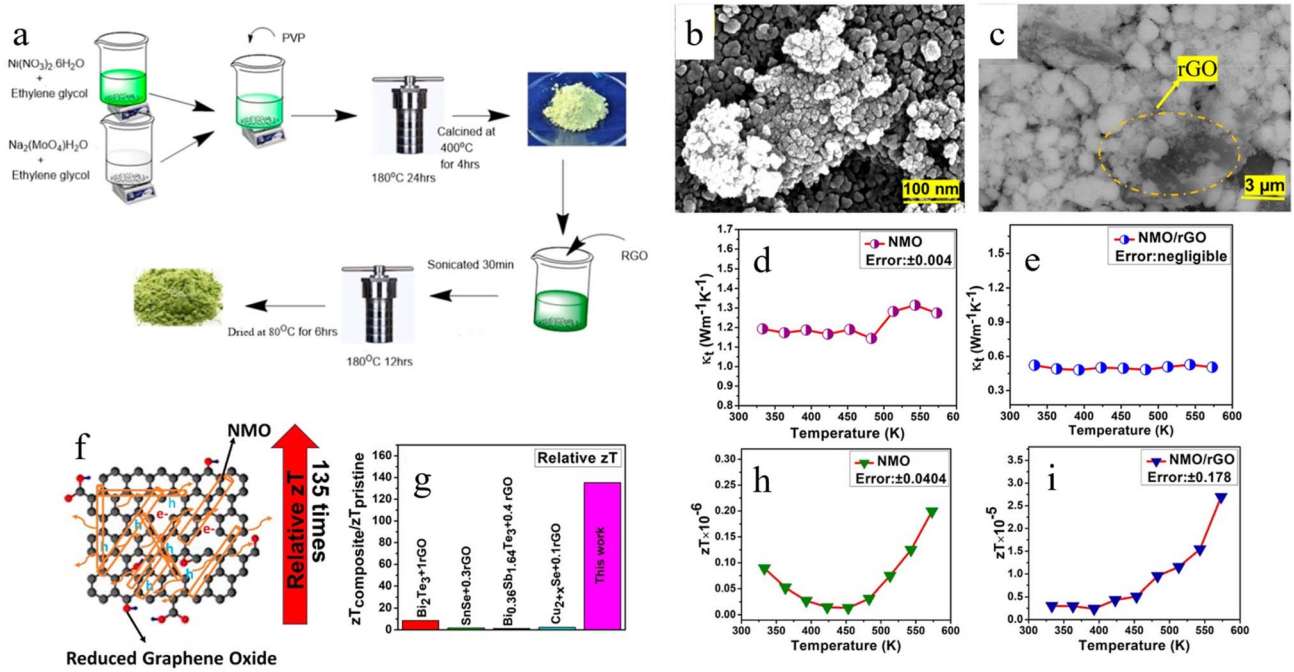

Fig. 11 (a) Schematic diagram of the preparation process of NMO/rGO. (b) FESEM image of NMO/rGO nanocomposites with a resolution of 100 nm, (c) rGO flakes in NMO/rGO nanocomposites, HRSEM image. (d and e) Comparison of total thermal conductivity between MMO and MMO/rGO nanocomposites. (f) Schematic diagram of carrier propagation in NMO/rGO nanocomposites, (g) relative *ZT* values of different materials combined with rGO. (h and i) *ZT* values of NMO and NMO/rGO nanocomposites at various temperatures. Reproduced from ref. 77 with permission. Copyright 2024 the American Chemical Society.

Open Access Article. Published on 28 July 2025. Downloaded on 12/27/2025 3:34:44 PM.
This article is licensed under a Creative Commons Attribution-NonCommercial 3.0 Unported Licence.

this temperature range, the thermoelectric properties fade quickly.

The thermal window period of $SrTiO_3$ is above 700 °C, which means that its application range as a thermoelectric material is limited.

In Lin Yue *et al.*'s article,[81] the influence of graphene doping on the thermoelectric properties of composite materials was further analyzed. They found that the addition of graphene oxide had a better effect on the performance of La doped $SrTiO_3$ (LSTO) than graphene. They used two different degrees of oxidation of graphene and sintered it with LSTO in two environments (with/without reduction using carbon powder). Fig. 12a–i show the effect of the addition of different mass fractions of graphene on the thermoelectric properties of La doped $SrTiO_3$ (LSTO). Finally, the experiment found that the thermoelectric properties of composite materials with mild graphene oxide added were better than those with severe graphene added. At the same time, they also found through experiments that the material produced under the conditions of carbon powder sacrificial bed reduction during the sintering process has the highest electrical conductivity, and the thermoelectric performance is also the most excellent. They speculate that the addition of graphene oxide first forms grain boundary barriers due to the presence of oxygen, which to some extent increases phonon scattering and reduces the thermal conductivity of the material. Overall, it has a higher *ZT* value than LSTO composite materials with graphene added. However, the addition of oxygen not only hinders the propagation of phonons, but also hinders the propagation of electrons in the material, reducing the conductivity. The advantages of mild oxidized graphene are not significant. So they reduced the oxygen in the oxidized graphene by using carbon powder (graphene powder was selected to eliminate variables) during the sintering process, forming more oxygen vacancies and improving the conductivity. This has significantly improved the thermoelectric properties of the material.

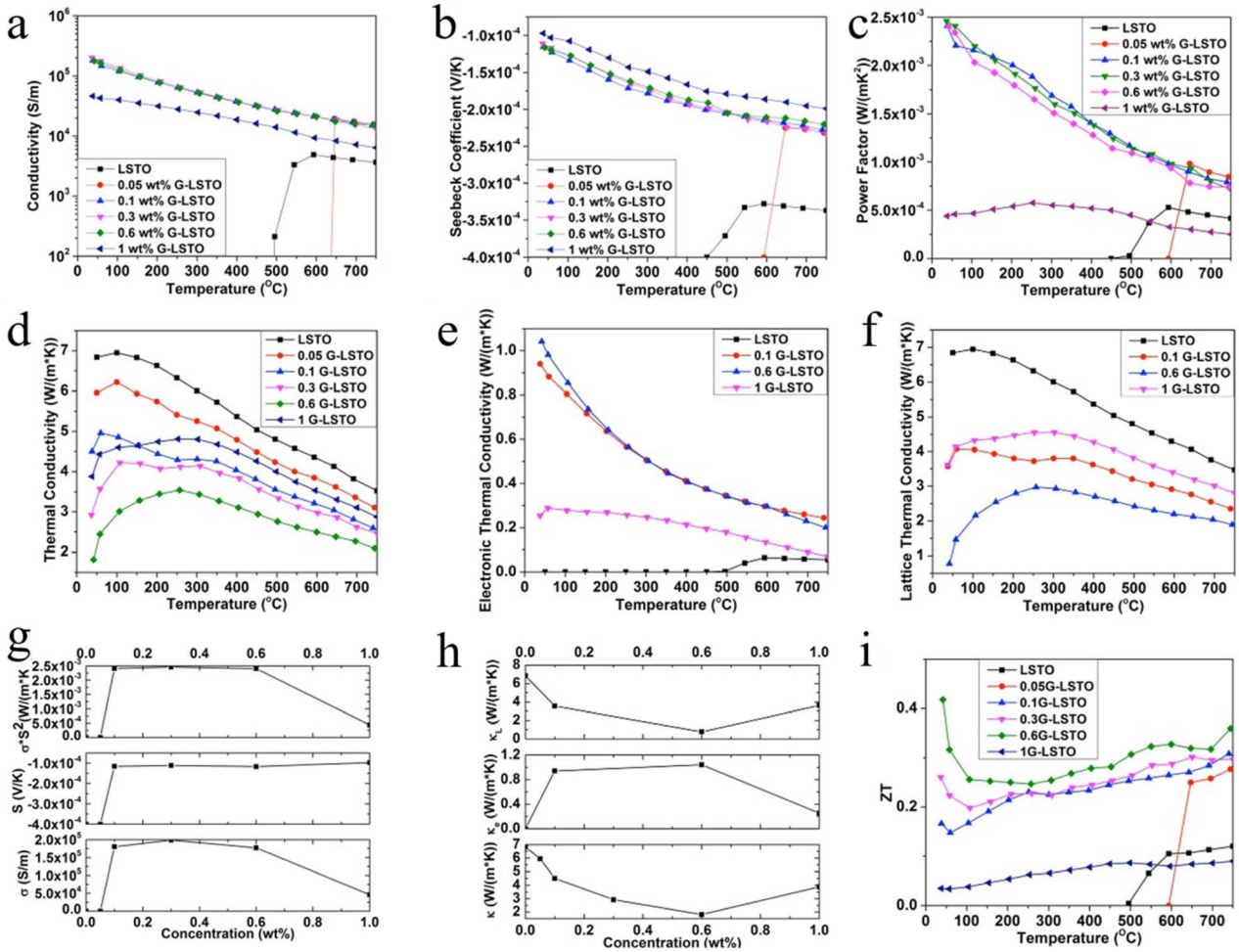

Fig. 12 Thermoelectric properties of LSTO and its nanocomposites with graphene: (a) electrical conductivity as a function of temperature, (b) Seebeck coefficient as a function of temperature, (c) power factor as a function of temperature, and (d) total thermal conductivity as a function of temperature. (e) Electronic thermal conductivity as a function of temperature, (f) lattice thermalconductivity as a function of temperature, and (g) electrical conductivity, Seebeck coefficient, and power factor against concentration of graphene at room temperature. (h) Thermal conductivity at room temperature as a function of graphene concentration. (i) Thermoelectric figure of merit for LSTO and the nanocomposites: *ZT* as a function of temperature. Reproduced from ref. 81 with permission. Copyright 2015 the American Chemical Society.

 © 2025 The Author(s). Published by the Royal Society of Chemistry

Open Access Article. Published on 28 July 2025. Downloaded on 12/27/2025 3:34:44 PM.
This article is licensed under a Creative Commons Attribution-NonCommercial 3.0 Unported Licence.

In the article by Dursun Ekren *et al.*,[82] the effect of chemical modification of graphene on the thermoelectric properties of composites was further analyzed. Researchers found that the addition of graphene oxide (GO) improved the performance of La-hybridized $SrTiO_3$ (LSTO) more significantly than that of pristine graphene. They used two graphenes with different degrees of oxidation, which were sintered with LSTO in two environments (with and without carbon powder for reduction). Finally, it is found that the thermoelectric properties of composites with light graphene oxide are better than those with heavy graphene oxide. Fig. 13a–h show the effect of the addition of different mass fractions of graphene oxide on the thermoelectric properties of La doped $SrTiO_3$ (LSTO). At the same time, they also found that the materials prepared under the condition of carbon powder sacrificial powder bed reduction in the sintering process have the highest electrical conductivity and the best thermoelectric performance. They speculate that the addition of graphene oxide first forms a grain boundary barrier due to the presence of oxygen, which increases phonon scattering to a certain extent, reduces the thermal conductivity of the material, and generally has a higher *ZT* value than the LSTO composites with graphene. However, the addition of oxygen hinders the propagation of phonons on the one hand, and the propagation of electrons in the material on the other, reducing the conductivity. The advantages of mild graphene oxide are not obvious. They then reduced the oxygen in graphene oxide with a carbon powder (graphene powder was chosen to eliminate variables) during the sintering process, creating more oxygen vacancies and improving conductivity. The result is a significant advantage in the thermoelectric properties of the material.

The previous section introduced the improvement in thermoelectric properties of lanthanum doped strontium titanate after the addition of graphene and graphene oxide, due to the excellent thermoelectric properties of lanthanum doped strontium titanate. However, the conductivity of strontium titanate is poor, so people have made a lot of efforts and attempts to improve the conductivity of strontium titanate based materials.[83] Jana *et al.*[84] improved the conductivity of graphene by modifying it with Fe_2O_3 on the basis of niobium doped strontium titanate, resulting in better conductivity enhancement than graphene oxide doped. They synthesized $SrTi_{0.85}Nb_{0.15}O_3$ (STN) using solid-phase method, and added Fe_2O_3 nanoparticle powder and graphene powder together in ethanol. After ultrasonic dispersion, ethanol was removed in an oven to obtain dried Fe_2O_3 modified graphene powder (FGR). Then mix FGR powder and STN powder thoroughly and use discharge plasma sintering to obtain experimental samples. By analyzing the FESEM images, they found that the composite material crystals were layered and had fractures in some areas (as shown by the yellow circle in Fig. 14b). This was due to the presence of FGR in the crystal layers, which caused grain boundaries. Due to the addition of Fe_2O_3, nano Fe_2O_3 particles were also found at some grain boundary edges. Further analysis of the thermoelectric performance (as shown in Fig. 14c–g) shows that the addition of FGR powder leads to a significant increase in conductivity (as shown in Fig. 14f), which also results in a significant improvement in power factor and hot spot quality with the addition of different amounts of FGR. This may be due to the addition of Fe_2O_3 leading to the formation of more oxygen vacancies near the grain boundaries, which helps carriers cross the grain boundaries and reduces the potential barrier between them. Meanwhile, the addition of FGR leads to an increase in lattice defects at the grain boundaries, hindering the transport of phonons and reducing the thermal conductivity of the sample (as shown in Fig. 14a). Finally, the thermal conductivity of niobium doped strontium titanate modified with Fe_2O_3 decreased by 34% and the optimal *ZT* value increased by 240%.

3.5 Others

In addition to being compounded with metal oxides such as nickel titanate and strontium titanate, graphene can also

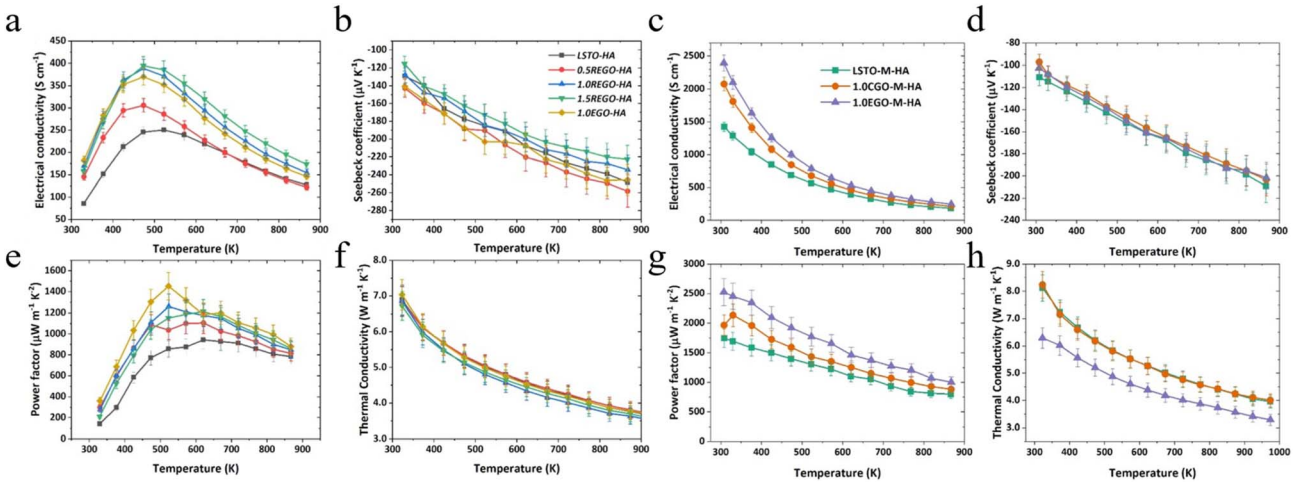

Fig. 13 Sintering samples under H_2 Ar flow without sacrificing powder, (a) conductivity, (b) Seebeck coefficient, (c) power factor, (d) thermal conductivity; the sample is sintered in the presence of H_2–Ar gas flow and sacrificial powder, with (e) conductivity, (f) Seebeck coefficient, (g) power factor, (h) thermal conductivity; Reproduced from ref. 82 with permission. Copyright 2022 published by American Chemical Society under a CC-BY license.

Open Access Article. Published on 28 July 2025. Downloaded on 12/27/2025 3:34:44 PM.
This article is licensed under a Creative Commons Attribution-NonCommercial 3.0 Unported Licence.

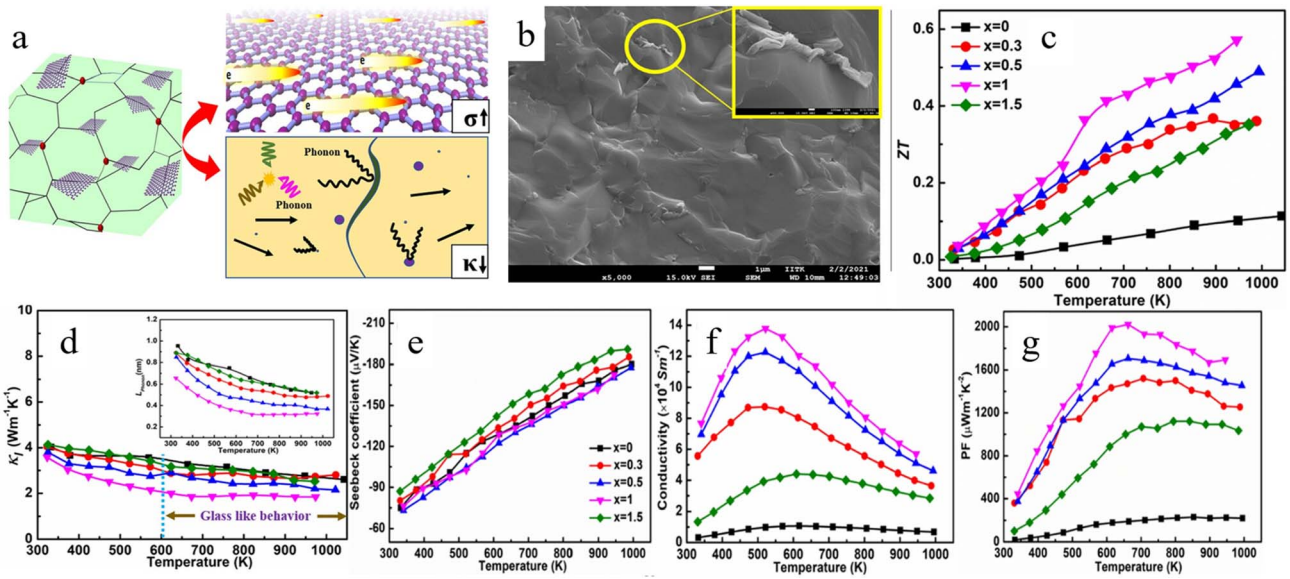

Fig. 14 (a) Schematic diagram of crystal structure and internal electron transport and phonon conduction of STN + FGR composite material; (b) FESEM image of fracture surface caused by FGR in STN + 1 wt% FGR composite crystal; (c) the thermoelectric properties of STN + FGR composite materials with different FGR contents at different temperatures, (d) *ZT* value, (e) thermal conductivity (phonon mean free path (Lphonon) as a function of temperature in the illustration), (e) Seebeck coefficient, (f) electrical conductivity, and (g) power factor. Reproduced from ref. 84 with permission. Copyright 2023 the American Chemical Society.

Table 1 Typical reports on graphene/conductive polymer composites in thermoelectric applications in recent years

Main composite materials	Preparation method	Thermoelectric figure of merit (*ZT*) or power factor (PF)	References
Bi_2Te_3/graphene quantum dots (GQDs)	Solution synthesis + spark plasma sintering (SPS)	$ZT = 0.55$ (425 K)	59
Cu_2Se/graphene oxide (GO) + multi-walled carbon nanotubes (MWCNT)	Chemical reduction + mechanical grinding	PF = 1120 μW m^{-1} K^{-2} (450 °C)	63
Cu_2Se/BiCuSeO/graphene	Self-propagating high-temperature synthesis (SHS) + SPS	$ZT = 2.82$ (1000 K)	60
Cu_2Se/graphene nanoplates	Ball milling + melt-solidification	$ZT = 2.44$ (870 K)	90
$Bi_{1.7}Sb_{0.3}Te_3$/exfoliated graphene oxide (EOG)	3D printing + atmosphere sintering	$ZT = 0.71$ (448 K)	71
Bi_2Te_3/Te–Se composite	3D printing + combustion sintering	$ZT \approx 0.85$ (473 K)	67
$SrTi_{0.85}Nb_{0.15}O_3/Fe_2O_3$-functionalized graphene (FGR)	Spark plasma sintering (SPS)	$ZT = 0.57$ (947 K)	84
$La_{0.67}Sr_{0.9}TiO_3$/graphene	Atmosphere sintering	$ZT = 0.42$ (300 K)	81
$La_{0.9}Sr_{0.8}TiO_3$/graphene oxide	Reducing atmosphere sintering	PF = 2525 μW m^{-1} K^{-2} (300 K)	82
NiMoO44/reduced graphene oxide	Solvothermal method	$ZT = 2.69 \times 10^{-5}$ (573 K)	77
ZnO/graphene oxide	One-step solution chemistry method	$ZT = 0.28$ (900 °C)	88
$LaCoO_3$/multilayer graphene	Mechanical milling + sintering	$ZT = 0.33$ (550 K)	87

improve the thermoelectric properties of metal oxides like lanthanum cobaltite and zinc oxide by enhancing electrical conductivity and reducing thermal conductivity.[85,86] Nithya Davis reported that[87] at 550 K, a lanthanum cobaltite composite doped with 0.08 wt% multilayer graphene achieved a *ZT* value of 0.33. Dongsheng Chen *et al.*[88] use reduced graphene oxide (rGO), by capturing Zn^{2+} ions and releasing additional electrons, increases the carrier concentration. When the rGO content is 1.5 wt%, the rGO/ZnO nanocomposite achieved a remarkable thermoelectric figure of merit of 0.28 at 900 °C, which is 8 times greater than that of pure ZnO and 60 times greater than that of aluminum-doped zinc oxide. More interestingly, Yiwei Cui *et al.*[89] reported the incorporation of graphene oxide as a filler into cement, linking the application of graphene in waste heat recovery with common building materials in daily life. The Table 1 below summarizes the thermoelectric effects of graphene and inorganic compound in recent years.

4 Graphene/conducting polymer composites

While graphene has received increasing attention in thermoelectric devices, some thermoelectric devices have also put

 © 2025 The Author(s). Published by the Royal Society of Chemistry

Open Access Article. Published on 28 July 2025. Downloaded on 12/27/2025 3:34:44 PM.
This article is licensed under a Creative Commons Attribution-NonCommercial 3.0 Unported Licence.

forward new requirements for the wearable performance of thermoelectric devices in areas such as human temperature difference power generation.[91] Graphene, as a traditional inorganic thermoelectric material, has been introduced earlier for its advantages in thermoelectric properties.[92,93] However, most inorganic materials are usually rigid, and their disadvantages in terms of ductility, elongation at break, and other properties limit their application in the field of wearable thermoelectric materials, and graphene is no exception.[94,95] So people thought of combining graphene with organic materials with high elongation at break to increase its application in wearable thermoelectric exchange devices.

4.1 Composite with PEDOT

Among various organic materials, polythiophene and its derivatives stand out due to their remarkable electrical properties, making some of them (such as poly(3-hexylthiophene), P3HT) promising candidates for thermoelectric research.[96] Within studies on the thermoelectric performance of the polythiophene family, materials based on PEDOT poly(3,4-ethylenedioxythiophene) are the most promising in the thermoelectric field.[69,97] Just like the copolymer or mixture of poly(3,4-ethylenedioxythiophene) and poly(phenylene sulfide) (PPS) (PEDOT:PSS), which has good conductivity and stability, it is a research thermoelectric device for wearable thermoelectric exchange.[98]

The development of graphene in the wearable field is closely related to PEDOT:PSS. Liu *et al.*[44] reported a study and application of graphene and PEDOT:PSS in the field of wearable thermoelectric technology. They mixed the dispersed graphene solution with PEDOT:PSS solution in proportion and then loaded it into a PTFE mold tube. After gelling, extrude the black hydrogel into ethanol to form polymeric fiber (as shown in Fig. 15a and b). The formed polymer fibers are further divided into two parts, one of which is immersed in an aqueous solution of polyethylene (PEIE) for a period of time. The semiconductor type of graphene/PEDOT:PS hybrid fibers treated with PEIE solution will be transformed from p-type to n-type. This is mainly due to the fact that PEIE solution contributes a large number of lone pair electrons of nitrogen atoms in its molecules to graphene when processing graphene/PEDOT:PS hybrid fibers. Move the Fermi level of the latter towards the valence band, completing the transition from p-type to n-type. This enables the thermoelectric converter to have a complete electronic transmission circuit. However, this significantly reduces the thermoelectric properties (as shown in Fig. 15e) and fracture elongation (as shown in Fig. 15f) of PEIE treated graphene/PEDOT:PS hybrid fibers. Overall, graphene/PEDOT:PS hybrid fibers have shown significant improvements in electrical conductivity and power factor, the PEDOT:PS composite with 70 wt% graphene (P_3G_7 hybrid fibers) loading demonstrated optimal thermoelectric performance (excluding the Seebeck coefficient). Notably, its electrical conductivity maintained a significant advantage over pristine graphene (as shown in Fig. 15c) even with increasing temperature (as shown in Fig. 15d). Particularly in the stress–strain curve used to evaluate the wearable performance of thermoelectric materials. The treatment of hybrid fibers with PEIE solution also enabled the successful transformation of graphene/PEDOT:PS hybrid fibers from p-type to n-type through the action of graphene without

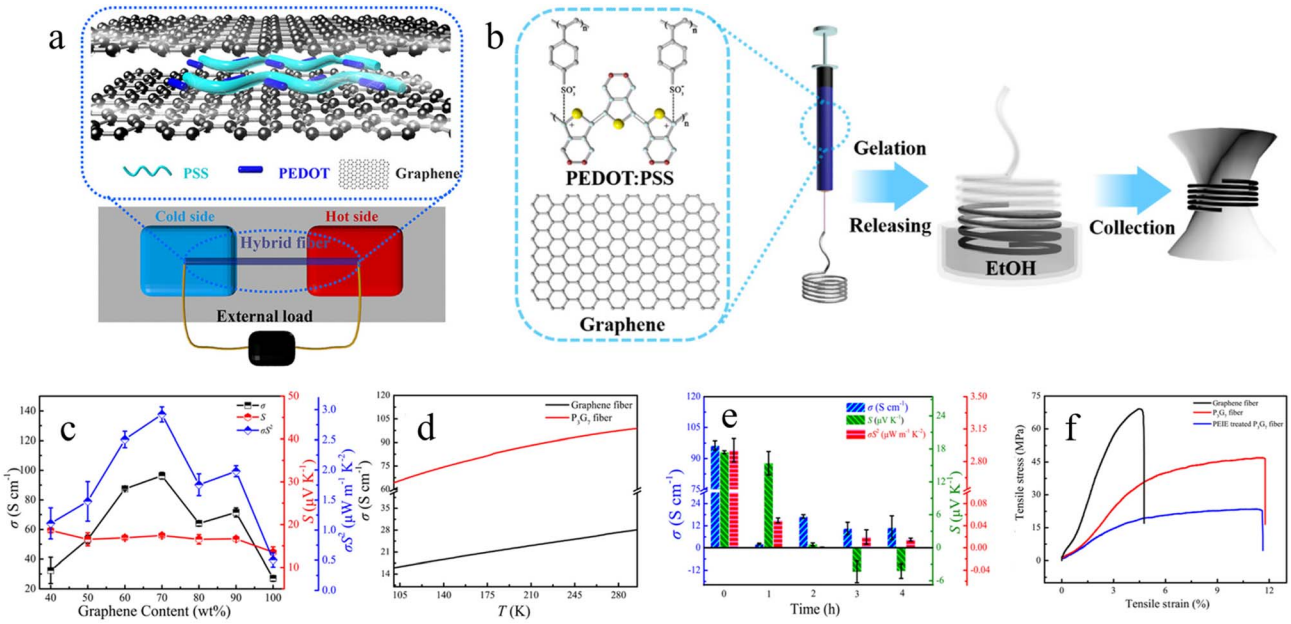

Fig. 15 (a) Schematic diagram of graphene/PEDOT:PS hybrid fiber structure and schematic diagram of thermoelectric device constructed based on it; (b) schematic diagram of graphene/PEDOT:PS hybrid fiber synthesis; (c) the thermoelectric properties of graphene/PEDOT:PSS fibers at different graphene contents; (d) the electrical conductivity of graphene and P_3G_7 hybrid fibers (PEDOT:PSS/graphene mass ratio of 3 : 7) at different temperatures; (e) the TE properties of P_3G_7 hybrid fibers treated with 37% PEIE solution for a period of time; (f) typical strain–stress curves of graphene, P_3G_7, and PEIE-P_3G_7 fibers. Reproduced from ref. 44 with permission. Copyright 2020 the American Chemical Society.

Open Access Article. Published on 28 July 2025. Downloaded on 12/27/2025 3:34:44 PM.
This article is licensed under a Creative Commons Attribution-NonCommercial 3.0 Unported Licence.

introducing other n-type semiconductor materials, constructing a complete thermoelectric device. However, the cost of this transformation is quite high, which has a negative impact on the overall thermoelectric conversion of the thermoelectric device.

For the doping modification of graphene, polyethyleneimine (PEI) solution was mentioned earlier. Some special organic solutions can be used to treat graphene, which was originally neutral, and turn it into an n-type or p-type semiconductor. This modification is interesting and can help construct a complete p–n structure thermoelectric converter.[99] Hyeon Jun Hwang *et al.*[43] reported a method for producing high power factor hybrid graphene thermoelectric converters by gradient doping of graphene. After using chemical vapor deposition method to deposit large areas of graphene on copper foil, the graphene was transferred to SiO_2/Si substrate by vacuum transfer method, and then the large area of graphene was divided into multiple strips. Dilute the dopants with ethanol (0.2 wt%) and lithium perchlorate (0.2 wt%) to prepare polyethyleneimine (PEI) and polyacrylic acid (PAA) solutions, and then immerse the graphene strips to obtain samples that can be used for detection (the preparation process is shown in Fig. 16a). Due to the positive charge of PEI, graphene treated with PEI is an n-type doped semiconductor. PAA carries a negative charge, and graphene treated with PAA is a p-type doped semiconductor. After testing the thermoelectric performance parameters of the samples (as shown in Fig. 16b–g), it was found that the fully processed graphene did not show any advantages in thermoelectric voltage, Seebeck coefficient, power factor, *etc.* Even after treatment with PEI solution, the power factor of graphene actually decreased (as shown in Fig. 16b–d). This may be due to the fact that the main charge carriers in graphene doped with PEI are still electrons, and the addition of PEI reduces the original conductivity. So the experimental report further carried out gradient doping treatment on graphene, that is, graphene strips were only full doped with PAA (as shown in Fig. 16h), or graphene strips were doped with PEI and PAA in half each (as shown in Fig. 16j). It can be observed that graphene treated with PAA semi doping has a significant improvement in power factor compared to fully doped graphene, which may be attributed to the enhancement of carrier gradient caused by the generation of hot carriers and Fermi level gradient. The Fermi level gradient under semi doped PAA is higher than that under fully doped PAA (as shown in Fig. 16i). Finally, under the optimal conditions of PAA doping, the power factor increased by 6 times compared to pure graphene. This study can provide assistance in the principles of graphene processing and semiconductor types for the construction of complete graphene containing hot spot converters in the future.

Efforts have been made in many aspects to further enhance the thermoelectric performance of graphene wearable devices. Among them, there is an exploration of the preparation process of graphene. A prevalent strategy involves utilizing graphene oxide (GO) as a substitute for pristine graphene. Xu *et al.*[100] developed a PEDOT-rGO nanocomposite with a distinctive pie-like architecture, where rGO nanosheets served as cores and PEDOT layers formed the shells. The realization of this hierarchical structure necessitates uniform polymeric coating of PEDOT on two-dimensional GO surfaces. In their methodology, Xu's team introduced EDOT monomers into an aqueous

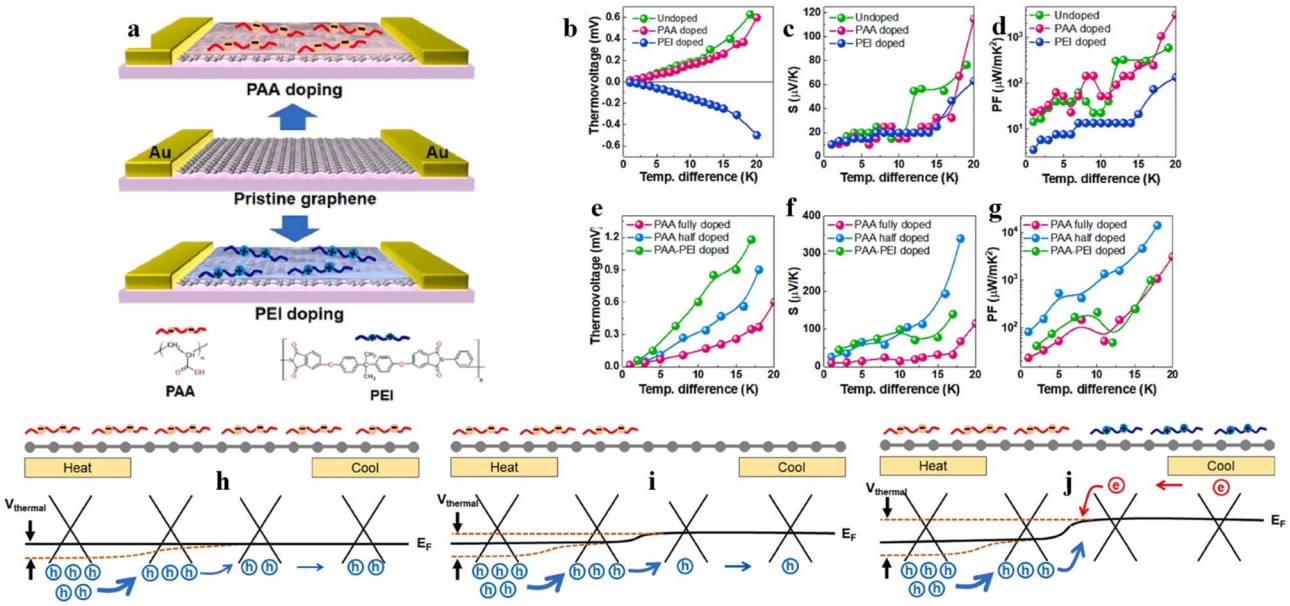

Fig. 16 (a) Schematic diagram of the preparation process of PAA/PEI doped graphene. The variation of thermoelectric performance with temperature difference under fully mixed conditions: (b) thermoelectric voltage; (c) Seebeck coefficient; (d) power factor. The variation of thermoelectric performance with temperature difference under gradient doping conditions: (e) thermoelectric voltage; (f) Seebeck coefficient; (g) power factor. Band alignment of the graphene thermoelectric devices under (h) full PAA doping, (i) half PAA doping, and (j) half PAA/half PEI doping. Reproduced from ref. 43 with permission. Copyright 2023 the Elsevier.

 © 2025 The Author(s). Published by the Royal Society of Chemistry

Open Access Article. Published on 28 July 2025. Downloaded on 12/27/2025 3:34:44 PM.
This article is licensed under a Creative Commons Attribution-NonCommercial 3.0 Unported Licence.

dispersion of rGO containing poly(sodium 4-styrenesulfonate) (PSS), followed by ultrasonication and stirring to facilitate EDOT adsorption onto rGO nanosheets. The interfacial adhesion between EDOT and rGO originates from π–π stacking interactions: the thiophene ring in EDOT constitutes an electron-rich aromatic system, while reduced graphene oxide (rGO) maintains sp^2-hybridized carbon domains with extensive π-conjugation in its non-oxidized regions. These conjugated domains, featuring delocalized π-electrons, establish strong π–π interactions with EDOT's thiophene rings. Subsequent *in situ* polymerization of adsorbed EDOT monomers on rGO surfaces yielded the final PEDOT-rGO nanocomposite with its characteristic pie-like morphology. This synthesis method is called template-directed *in situ* polymerization. Comprehensive characterization *via* SEM, TEM (Transmission Electron Microscopy), and AFM (Atomic Force Microscopy) techniques confirmed the homogeneity and thickness uniformity of PEDOT coatings on rGO substrates. Notably, the π–π interfacial coupling between rGO and PEDOT effectively mitigates conjugation defects commonly observed in conventional rGO/PEDOT composites, resulting in significantly reduced charge carrier hopping barriers and substantially enhanced carrier mobility. Furthermore, the disordered structure of rGO contributes to improved power factors compared to pristine graphene, collectively facilitating more efficient conductive pathways in the PEDOT-rGO nanocomposite. The optimized composite demonstrated a remarkable room-temperature power factor of $5.2 \pm 0.9 \times 10^{-6}$ W m^{-1} K^{-2}, representing a 13.3-fold enhancement over conventional PEDOT materials.

Another common method is to reduce oxidized graphene to obtain graphene for the preparation of thermoelectric devices.[27,101] However, Xiong *et al.*[102] further analyzed the defects of oxidized graphene and used liquid exfoliation to obtain graphene with even better performance. Thus, graphene PEDOT:PSS composite nanofilm (referred to as PG film) was fabricated. They used two dispersion solutions, dimethylformamide (DMF) and *N*-methyl-2-pyrolidone (NMP), and dispersed the raw materials under ultrasound to form a nano film on a porous polyvinylidene fluoride (PVDF) membrane by vacuum filtration (as shown in Fig. 17a). After drying in an oven, the sample that can be used for experimental detection was obtained (as shown in Fig. 17b) By controlling the amount of graphene added, it can be observed that compared to a single PEDOT:PSS film, the conductivity of PG composite film decreases with the increase of graphene content (as shown in Fig. 17c). This is because PEDOT:PSS film itself has a higher carrier concentration, while PG film has a lower carrier concentration. In other words, the addition of graphene reduces the carrier concentration of PG nanofilms, leading to a decrease in conductivity. However, from Fig. 17c, we can also observe that although the conductivity decreases with the addition of graphene, the Seebeck coefficient increases, and the final power factor (determined by the sum of the square of the Seebeck coefficient and the conductivity) increases with the addition of graphene, reaching its peak at a graphene mass fraction of 3%. This may be due to the addition of graphene, which forms new conjugated electron orbitals between graphene and PEDOT:PSS electron orbitals, providing favorable space for carrier transport. Secondly, graphene obtained by liquid exfoliation method has a more regular micro surface, with fewer defect sites on the surface compared to graphene reduced by oxidized graphene, which increases the carrier concentration of PG nanofilms. Next, the authors and their team treated PG nanofilms with 3% graphene (referred to as PG3) mass fraction using hydrazine.

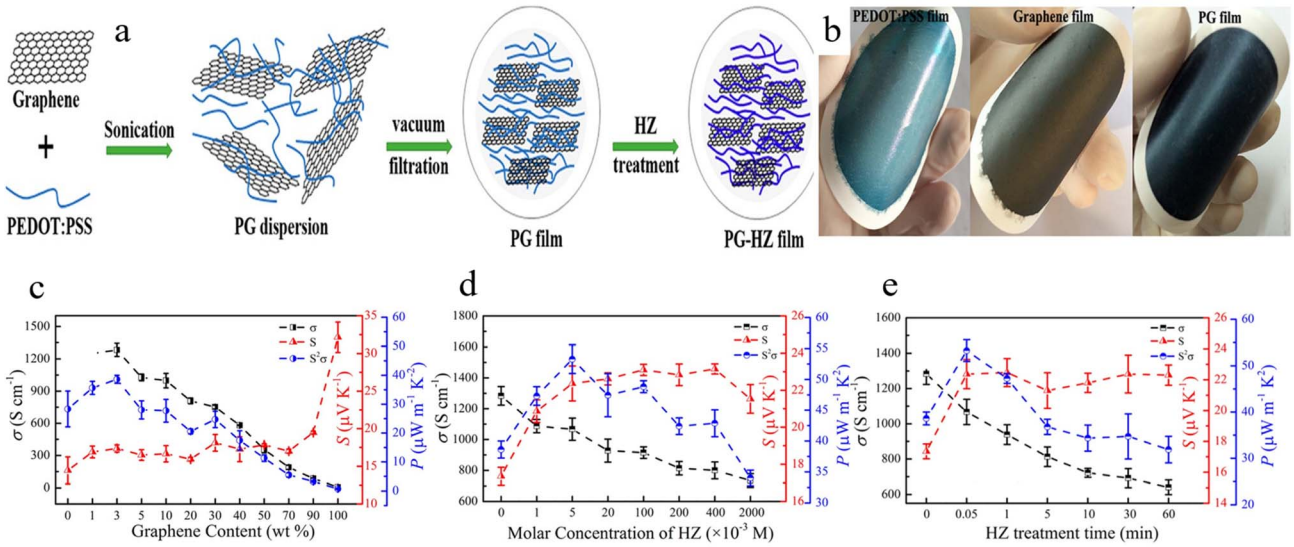

Fig. 17 (a) Schematic diagram of the preparation and hydrazine treatment process of PEDOT:PSS/graphene composite nanofilm; (b) physical photos of PEDOT:PSS, graphene, and PG films; (c) conductivity, Seebeck coefficient, and power factor plots of graphene with different component contents; (d) conductivity, Seebeck coefficient, and power factor plots of PG membranes immersed in hydrazine solutions of different concentrations; (e) conductivity, Seebeck coefficient, and power factor plots of PG films immersed in hydrazine solution for different durations. Reproduced from ref. 102 with permission. Copyright 2015 the American Chemical Society.

Open Access Article. Published on 28 July 2025. Downloaded on 12/27/2025 3:34:44 PM.
This article is licensed under a Creative Commons Attribution-NonCommercial 3.0 Unported Licence.

Measure a series of thermoelectric parameters of PG3 sample films immersed in hydrazine aqueous solutions of different concentrations and treatment times (as shown in Fig. 17d and e). They found that although hydrazine solution had adverse effects on conductivity with concentration and treatment time, the power factor of PG3 film reached its peak after treatment with hydrazine solution at a certain concentration for a period of time. This may be due to the strong reducibility of hydrazine, which increases the energy barrier for charge hopping between chains and domains, leading to a decrease in conductivity and an increase in Seebeck coefficient. Finally, the PG nanofilm treated with hydrazine achieved the optimal power factor of 53.3 $\mu W\ m^{-1}\ K^{-2}$ at the sacrifice of a certain conductivity, with an estimated ZT of 0.05 at room temperature.

For wearable thermoelectric materials, their main thermoelectric performance still relies on inorganic thermoelectric materials, especially for n-type wearable thermoelectric converters. Faced with the vast demand for waste heat conversion in the future, a large amount of n-type thermoelectric materials will be required. However, the elements required for the preparation of traditional inorganic thermoelectric materials, such as Te, Se, Ag, are mostly rare and expensive, and some of them are toxic to the human body, making them unsuitable for a wide range of application needs.[103] Wang *et al.*[104] proposed a ternary thin film wearable thermoelectric converter constructed using chalcopyrite, graphene, and PEDOT:PSS. Chalcopyrite, as a common mineral, has abundant reserves on Earth and is non-toxic. They added graphene and brass mineral powder to a mixed solution of PEDOT:PSS, ethanol, and distilled water after thorough grinding and mixing. After the solution is fully mixed, it is dropped onto a PET substrate using the drop casting method. After drying and cold pressing treatment, a ternary mixed film is obtained (as shown in Fig. 18a). After experimental performance testing, it was found that compared to binary films without graphene (containing only chalcopyrite and PEDOT:PSS), the addition of graphene increased the conductivity by about 4.3 times compared to the maximum value of binary films. This reflects the excellent performance of graphene in improving the conductivity of thermoelectric materials. From Fig. 18c, we can also see that with the initial increase of graphene content, the absolute values of the Seebeck coefficient, conductivity, power factor, and other coefficients of the ternary film show an increasing trend (the Seebeck coefficient changes to negative values, indicating that the addition of graphene does not change the semiconductor type of the composite film). However, as the graphene content continues to increase, these thermoelectric coefficients show a decreasing trend after reaching their peak. This is because excessive graphene can disrupt the overall carrier mobility of the material, which may be due to the aggregation of graphene in the matrix and the breaking of π–π conjugated interaction bonds between graphene and polymers. This indicates that graphene can only be added within an appropriate range to facilitate the construction of conductive networks in porous membranes (as shown in Fig. 18b). Further research in the article found that after adding a fixed amount of graphene, the content of chalcopyrite also affects the thermoelectric properties of graphene (as shown in Fig. 18d–f). The effect of chalcopyrite content on the thermoelectric properties of ternary films is similar to that of graphene. The performance shows a trend of decreasing as the content increases. The damage caused by excessive chalcopyrite to thermoelectric properties may be due to the increased interface potential barrier between chalcopyrite and graphene, which

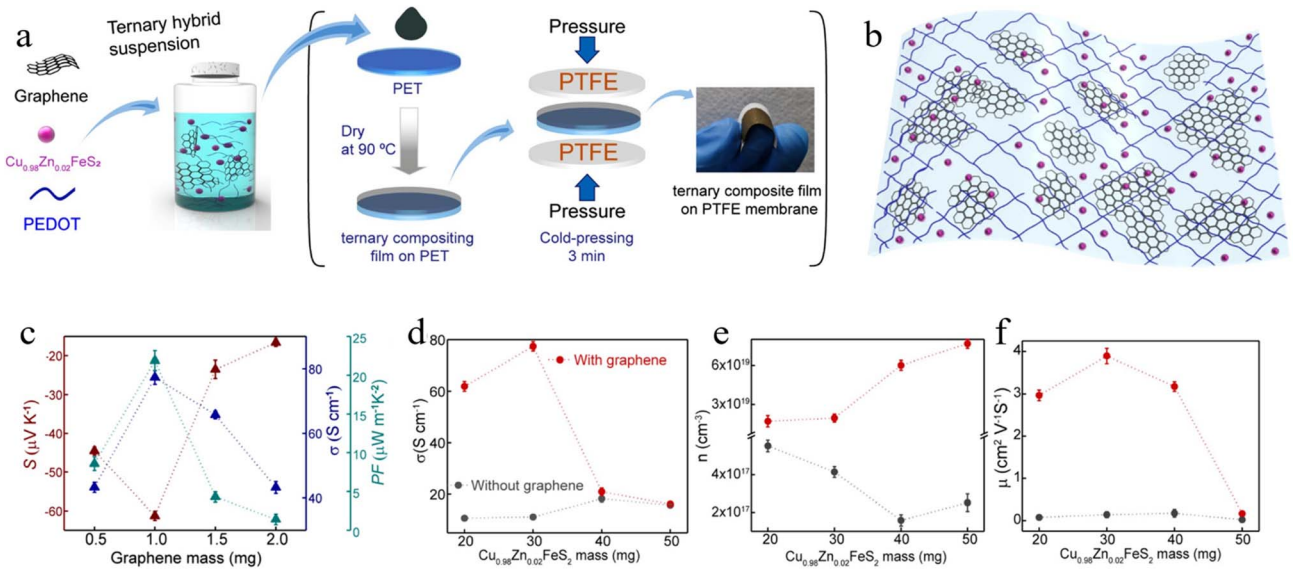

Fig. 18 (a) Preparation process and sample schematic diagram of $Cu_{0.98}Zn_{0.02}FeS_2$/PEDOT:PSS/graphene ternary thin film; (b) schematic diagram of the composition of $Cu_{0.98}Zn_{0.02}FeS_2$/PEDOT:PSS/graphene film; (c) the variation graphs of Seebeck coefficient, conductivity, and power factor of ternary thin films with graphene mass as the independent variable; the thermoelectric properties (d) Seebeck coefficient (e) carrier concentration (f) carrier mobility of binary and ternary films with different chalcopyrite contents. Reproduced from ref. 104 with permission. Copyright 2021 published by American Chemical Society under a CC-BY license.

 © 2025 The Author(s). Published by the Royal Society of Chemistry

Open Access Article. Published on 28 July 2025. Downloaded on 12/27/2025 3:34:44 PM. This article is licensed under a Creative Commons Attribution-NonCommercial 3.0 Unported Licence.

hinders the propagation of charge carriers. After selecting the optimal content ratio, the thermoelectric properties of the chalcopyrite/PEDOT:PSS/graphene ternary composite film obtained achieved an enhanced conductivity of about 77.4 S cm^{-1} and a maximum power factor of about 23.7 μW m^{-1} K^{-2}. In terms of wearable performance, after 2000 bending cycles, the thermoelectric performance of the ternary composite film can still maintain over 80% of its value. In terms of improvement, the article proposes that in the future, chemical synthesis can be used instead of grinding to obtain thermoelectric nanocrystals to control crystal size, and surface active agents can be used for capping or functional group grafting to improve the adverse effects of graphene aggregation.

4.2 Composite with polyaniline

Polyaniline (PANI) is a common conductive polymer material. Its monomer was synthesized and began to be studied in the early 20th century.[105] Due to its unique π-electron conjugated structure, polyaniline has a narrow bandgap, exhibiting good conductivity and dopability.[106] The segment structure of the polymer also provides ample space for doping, offering significant potential for enhancing conductivity.[107] In practical applications of thermoelectric materials, polyaniline has recently garnered widespread attention, particularly in the development of thermoelectric converters, especially wearable ones, owing to the unique flexibility of polymer materials.[108] Graphene, as an excellent thermoelectric doping material, is also closely associated with polyaniline. Liming Wang *et al.*[109] reported the composite of three-dimensional tubular graphene with polyaniline.

Nathan D. Wood *et al.*[110] used density functional theory to calculate the thermoelectric properties of composites composed of graphene, polyaniline, and strontium titanate. Graphene is widely and uniformly distributed in polyaniline, significantly increasing the electrical conductivity of the conductive polymer. Compared to pure polymers, the conductivity can be improved by two orders of magnitude. This is primarily due to the formation of a conductive network by the extensive and uniform distribution of graphene in polyaniline, which reduces the potential barrier required for carrier hopping between different segments. Additionally, the addition of graphene causes noticeable agglomeration in polyaniline, hindering phonon propagation and reducing thermal conductivity. The role of graphene in polyaniline is also evident in that polyaniline can act as a bridge and binder, effectively connecting graphene with inorganic semiconductor materials, thereby enhancing the conductivity of the semiconductor materials and imparting a "metallic" character. Lin *et al.*[111] reported a simple and environmentally benign one-step chemical synthesis of *p*-phenylenediamine-modified graphene (PDG), which was subsequently copolymerized with aniline to fabricate a novel PDG/polyaniline semi-interpenetrating network (S-IPN) conductive polymer composite. The study revealed that the chemically bonded PDG and PANI in the S-IPN structure created additional charge transport pathways. This innovative design eliminated the conventional requirement of incorporating large amounts of graphene to establish conductive networks for enhancing electrical conductivity. Remarkably, the composite achieved effective improvement in overall conductivity and Seebeck coefficient (thus thermoelectric performance) with only a few percent of graphene content.The optimized PDG/polyaniline composite containing 3 wt% PDG demonstrated a peak thermoelectric figure of merit (*ZT*) of 0.74 at 80 °C. This performance represents a significant advancement in developing high-efficiency thermoelectric materials with minimal graphene loading. In addition to binary composites of graphene and polyaniline, Costa *et al.*[112] synthesized a ternary conductive polymer composite of acrylic acid (ACR), graphene (GR), and polyaniline (PANI) *via in situ* polymerization. Experimental measurements revealed that this ACR/GR/PANI ternary composite achieved a maximum power factor of 4.94 μW m^{-1} K^{-1} at room temperature.

In the thermoelectric modification of graphene-composite polyaniline materials, leveraging the unique polymer structure and potential doping space of polyaniline, Ali *et al.*[113] utilized this characteristic to modify graphene by doping reduced graphene oxide with nitrogen and sulfur, preparing an n-type reduced graphene oxide/polyaniline (rGO/PANI) semiconductor. A mere 1% mass fraction of graphene doping can significantly improve the thermoelectric properties of the composite material. The final prepared PANI nanocomposite containing 1 wt% sulfur and nitrogen co-doped rGO exhibited a Seebeck coefficient, power factor, and *ZT* value of −1.75 mV K^{-1}, 95 μW m^{-1} K^{-2}, and 0.06, respectively.

In the specific application of wearable thermoelectric devices, polyaniline can also be combined with treated cotton fabrics. Anshu Panbude *et al.*[114] reported a two-step method involving *in situ* polymerization and solution blending to prepare highly conductive and flexible cotton fabrics. The composite of polyaniline and graphene was uniformly coated on the surface of the cotton fabric *via* a solution method. The conductive network constructed by graphene and polyaniline was evenly dispersed on the cotton fabric surface, providing excellent conductivity. Additionally, it exhibited good UV shielding properties. Ultimately, at the optimal temperature, the thermal power value of the PANi/graphene composite fabric reached 0.045 μV K^{-1}.

It is evident that polyaniline, as a high-performance conductive polymer, holds significant potential in wearable thermoelectric applications, primarily due to its unique molecular structure. After doping with graphene, its conductivity is greatly enhanced by the conductive network formed between graphene and polyaniline.[115–117] Further doping of graphene with elements such as nitrogen and sulfur can increase the carrier concentration within polyaniline. In terms of thermal conductivity, polyaniline's semi-crystalline nature and highly disordered structure result in low thermal conductivity. When compounded with graphene, the interfaces encountered by phonons during propagation are further increased, enhancing phonon scattering.[118] Polyaniline can also act as an adhesive in wearable thermoelectric converters, adhering well to other material surfaces and providing greater space for the thermoelectric application of graphene.

Open Access Article. Published on 28 July 2025. Downloaded on 12/27/2025 3:34:44 PM.
This article is licensed under a Creative Commons Attribution-NonCommercial 3.0 Unported Licence.

4.3 Composite with polypyrrole

Polypyrrole (PPy), another conductive polymer, also exhibits significant advantages in the thermoelectric field. Its low thermal conductivity helps maintain a large temperature gradient, thereby improving thermoelectric conversion efficiency.[119] Additionally, the conductivity of polypyrrole can be optimized through doping and structural regulation, enabling it to exhibit good electrical conductivity in thermoelectric materials.[120] As an organic polymer, polypyrrole's large molecular chains allow for the control of its morphology as needed, offering excellent plasticity.[121] For example, different types of surfactants can be added to control the synthesis of polypyrrole nanoparticles, nanotubes, and nanowires.[122] Du *et al.*[123] used a soft template polymerization method to prepare polypyrrole nanowire/graphene thermoelectric composites. Experiments showed that when the PPy nanowire content was 20 wt%, the PPy nanowire/graphene composite achieved a maximum power factor of 1.01 μW m^{-1} K^{-2} at ~380 K, which is 3.3 times that of pure PPy nanowires.

Polypyrrole can also be coated on graphene particles. Ajit Debnath *et al.*[124] introduced a method using ultrasound-assisted *in situ* oxidative polymerization to prepare NiO-bound polypyrrole-coated graphene (NiO@PPy/Gr) composites. The study found that graphene (Gr) plays a crucial role in the NiO@PPy/Gr composite. Firstly, the π–π interaction between the π-bond surface of graphene and the conjugated structure of polypyrrole not only enhances the ordered arrangement of PPy molecular chains but also reduces π–π conjugation defects, thereby improving carrier mobility and conductivity. Secondly, graphene, as a highly conductive material, provides efficient transport channels for carriers, further enhancing the composite's conductivity. Additionally, the introduction of NiO nanoparticles acts as a conductive bridge between PPy and graphene, promoting carrier hopping between the two and reducing the hopping barrier, thereby enhancing carrier transport efficiency. The presence of graphene also makes the arrangement of PPy molecular chains more ordered, reducing chain twisting and further enhancing carrier mobility. Ultimately, these synergistic effects enable the NiO@PPy/Gr composite to achieve a power factor of 28.22 μW m^{-1} K^{-2} at a temperature difference of 100 °C, which is 855 times that of pure PPy and 15.7 times that of PPy/Gr. The introduction of graphene not only optimizes the material's molecular structure but also significantly enhances thermoelectric performance, providing new insights for the performance optimization of polymer-based thermoelectric materials. Han *et al.*[125] also employed an *in situ* polymerization approach to fabricate reduced graphene oxide (rGO)/polypyrrole (PPy) composites with sodium dodecyl sulfate (SDS) as a surfactant. The specific methodology was similar to the aforementioned process, ultimately yielding uniformly coated rGO/PPy composites. The resulting material demonstrated significantly enhanced thermoelectric performance, achieving a remarkable room-temperature power factor of 3.01 μW m^{-1} K^{-2}, which represents an 84-fold improvement compared to pristine PPy.

Of course, graphene can also be compounded with various organic materials. Yihan Wang *et al.*[126] studied ternary composite thermoelectric materials of graphene, polyaniline, and polypyrrole, as well as graphene, polyaniline, and polydopamine. They found that the molecular chains of PPy are more ordered on the graphene surface, reducing the resistance to carrier transport and further enhancing conductivity. Similarly, PANI is deposited and arranged on the composite surface, making the PANi molecular chains more extended and ordered, reducing the potential barrier for carrier hopping and improving carrier mobility. This is likely due to the combined method of *in situ* polymerization and solution treatment used in the experiment, which allows PPy and PANI to be uniformly dispersed on the graphene surface. The similar chain structures of PANI and PPy further enhance conductivity through synergistic effects. However, the significant improvement in conductivity is primarily attributed to the efficient conductive network formed by graphene. The Table 2 below summarizes the thermoelectric effects of graphene and macromolecular organic compound in recent years.

4.4 Composite with organic small molecules

Although the composite of graphene with organic compounds is mostly composed of conductive polymer organic compounds, the unique two-dimensional structure and microscopic size of graphene also allow it to bind well with small molecule organic compounds such as tetracyano benzoquinone dimethyl (TCNQ) and tetrafluorotetracyano benzoquinone dimethyl (F4-TCNQ)[127] and phthalocyanine (Pc).[128] Among them, small molecule organic compounds play a role in modifying the edges or surfaces of graphene. In this regard, there is relatively little experimental research and more theoretical calculation research. Yao *et al.*[129] used molecular dynamics simulation combined with non-equilibrium Green's function (NEGF) form, and the Atomistic ToolKit (ATK) 2019 software package to calculate electron transfer coefficients (such as conductivity, Seebeck coefficient, and electron thermal conductivity). They calculated the *ZT* value of cor4GNRs of cyclobutadiene graphene nanoribbons (cor44GNRs) at room temperature, which exceeded 2.1, due to their extremely low thermal conductivity (12 W m^{-1} K^{-1}) and relatively high conductivity and Seebeck coefficient. Graphene nanoribbons (GNRs) have significantly reduced thermal conductivity compared to graphene due to edge scattering effects, and cor4GNRs are a novel type of graphene nanoribbon with a unique edge structure composed of carbon clusters saturated with hydrogen and oxygen atoms, connected by quaternary carbon rings. This structure is rougher than traditional graphene nanoribbons and has unique edge functional groups. The unique edge structure causes boundary scattering effects, rather than phonon scattering of quaternary rings. By comparing the thermal conductivity of linear GNRs and cor4GNRs, it was found that the thermal conductivity of cor4GNRs was significantly lower than that of traditional serrated and armchair GNRs. The above work provides ideas for the future development of graphene in the thermal power field. Compared to time-consuming and repetitive experiments, computational simulations can help

 © 2025 The Author(s). Published by the Royal Society of Chemistry

Open Access Article. Published on 28 July 2025. Downloaded on 12/27/2025 3:34:44 PM. This article is licensed under a Creative Commons Attribution-NonCommercial 3.0 Unported Licence.

Table 2 Typical reports on graphene/conducting polymer composites for thermoelectric application in recent years

Materials composed	Preparation method	Thermoelectric figure of merit (*ZT*) or power factor (PF)	References
$Cu_{1-x}Zn_xFeS_2$/PEDOT:PSS/graphene	Drop-casting and cold-pressing	PF: 23.7 μW m^{-1} K^{-2}	104
PEDOT:PSS/graphene	Vacuum filtration	PF: 53.3 μW m^{-1} K^{-2}	102
Graphene/PEDOT:PSS	Hydrothermal process	PF: 2.0 μW m^{-1} K^{-2}	44
Graphene oxide/PEDOT:PSS	*In situ* polymerization	PF: 5.2 μW m^{-1} K^{-2}	100
Diamino-modified graphene/polyaniline	Chemical route	*ZT*: 0.74	111
PANI/graphene/acrylic matrix	*In situ* polymerization	PF: 4.94 μW m^{-1} K^{-2}	112
Graphene/PANi	*In situ* polymerization	PF: 92.17 μW m^{-1} K^{-2}	114
Polypyrrole/graphene/polyaniline	*In situ* polymerization and solution process	PF: 52.5 μW m^{-1} K^{-2}	126
3D graphene/polyaniline	Composite preparation	*ZT*: 0.02	109
PDA/graphene/PANi	*In situ* polymerization	PF: 92.17 μW m^{-1} K^{-2}	20
Nitrogen/sulfur-doped rGO/PANI	Hydrothermal synthesis, *in situ* chemical oxidative polymerization	PF: 95 μW m^{-1} K^{-2}	113
Polypyrrole nanowires/graphene	Soft template polymerization	PF: 1.01 μW m^{-1} K^{-2} (at 380 K)	123
NiO@polypyrrole/graphene	*In situ* oxidative polymerization, ultrasound-assisted	PF: 28.22 μW m^{-1} K^{-2}	124
Graphene oxide/polypyrrole	*In situ* polymerization	PF: 3.01 μW m^{-1} K^{-2}	125

researchers design, calculate, and optimize test protocols more efficiently, offering intuitive insights into material structures. Especially in today's era of artificial intelligence, the use of computers for theoretical calculations of material properties will be a major trend in the future.[130,131]

5 Conclusion and outlook

Currently, graphene-based composite materials have made significant progress in optimizing thermoelectric performance through doping, functionalization, and nanostructure design. For instance, by introducing quantum confinement effects, interface engineering, and heterostructure construction, the trade-off between electrical conductivity and thermal conductivity has been effectively balanced, leading to a substantial improvement in the thermoelectric figure of merit (*ZT*). However, despite the enhanced thermoelectric conversion efficiency of existing materials, they still fall short of meeting the demands for large-scale commercial applications and industrial waste heat recovery. This limitation stems from the high cost of rare earth elements required for most thermoelectric materials, the environmental toxicity of some materials, and the narrow thermoelectric operating windows of others. The practical application of graphene in the thermoelectric field still faces numerous challenges. These challenges also represent future directions for the development of graphene-based thermoelectric materials:

(1) Multi-scale collaborative design: by integrating graphene's nanostructures (such as nanoribbons and quantum dots) with macroscopic composite systems (*e.g.*, polymer/graphene, inorganic semiconductor/graphene), it is possible to synergistically optimize carrier transport and phonon scattering at the atomic, nanoscale, and macroscopic levels, achieving decoupled control of electrical and thermal transport properties.[118]

(2) Novel functionalization strategies: in-depth exploration of chemical doping, defect engineering, and surface modification techniques will further enhance graphene's Seebeck coefficient and reduce lattice thermal conductivity.

(3) Flexible devices and integrated applications: graphene's mechanical flexibility and chemical stability provide unique advantages for the development of flexible thermoelectric devices. In the future, graphene-based flexible thermoelectric films and fibers could be widely applied in wearable electronics, self-powered sensors, and smart textiles,[20] enabling continuous energy harvesting from the temperature difference between the human body and the environment, thereby driving innovations in the Internet of Things (IoT) and smart healthcare.[19]

(4) Green synthesis and industrialization breakthroughs: developing low-cost, low-energy green synthesis processes for graphene (such as biomass carbon source conversion[132] and electrochemical exfoliation[133–135]) and enhancing its compatibility with existing industrial systems are key to realizing the large-scale application of graphene-based thermoelectric materials. Additionally, integrating artificial intelligence and high-throughput computing to accelerate the screening and design of novel graphene composites will significantly shorten the research and development cycle.[130,131]

Data availability

No primary research results, software or code have been included and no new data were generated or analyzed as part of this review.

Conflicts of interest

The authors declare no competing financial interest.

Acknowledgements

This research was financially supported by Innovation Capability Improvement Project of Science and Technology smes of Shandong Province (Grant No. 2024TSGC0935).

Open Access Article. Published on 28 July 2025. Downloaded on 12/27/2025 3:34:44 PM.
This article is licensed under a Creative Commons Attribution-NonCommercial 3.0 Unported Licence.

References

1 D. Beretta, N. Neophytou, J. M. Hodges, M. G. Kanatzidis, D. Narducci, M. Martin-Gonzalez, M. Beekman, B. Balke, G. Cerretti and W. Tremel, *Mater. Sci. Eng., R*, 2019, **138**, 100501.
2 D. Wei and J. Kivioja, *Nanoscale*, 2013, **5**, 10108–10126.
3 H. Alam and S. Ramakrishna, *Nano energy*, 2013, **2**, 190–212.
4 S. Twaha, J. Zhu, Y. Yan and B. Li, *Renewable Sustainable Energy Rev.*, 2016, **65**, 698–726.
5 T. A. Amollo, G. T. Mola, M. S. K. Kirui and V. O. Nyamori, *Crit. Rev. Solid State Mater. Sci.*, 2017, **43**, 133–157.
6 R. Mulla, A. O. White, C. W. Dunnill and A. R. Barron, *Energy Adv.*, 2023, **2**, 606–614.
7 M. Y. Zhu, C. C. Lu and L. R. Liu, *iScience*, 2023, **26**, 106718.
8 Y. Xu, W. Zhang, J. Shi, X. Zou, Y. Li, H. E. Tahir, X. Huang, Z. Li, X. Zhai and X. Hu, *Food Chem.*, 2017, **237**, 423–430.
9 W. Zhang, Y. Xu and X. Zou, *Food Chem.*, 2018, **261**, 1–7.
10 Z. Ding, C. Du, W. Long, C.-F. Cao, L. Liang, L.-C. Tang and G. Chen, *Sci. Bull.*, 2023, **68**, 3261–3277.
11 G. Li, Y. Hu, J. Chen, L. Liang, Z. Liu, J. Fu, C. Du and G. Chen, *Adv. Funct. Mater.*, 2023, **33**, 2303861.
12 Q. Sun, C. Du and G. Chen, *Prog. Mater. Sci.*, 2025, **149**, 101402.
13 C. Du, M. Cao, G. Li, Y. Hu, Y. Zhang, L. Liang, Z. Liu and G. Chen, *Adv. Funct. Mater.*, 2022, **32**, 2206083.
14 L. Luo, S. Ma, L. Li, X. Liu, J. Zhang, X. Li, D. Liu and T. You, *Food Chem.*, 2019, **292**, 98–105.
15 A. S. Sharma, S. Ali, D. Sabarinathan, M. Murugavelu, H. Li and Q. Chen, *Compr. Rev. Food Sci. Food Saf.*, 2021, **20**, 5765–5801.
16 S. Wu, N. Duan, Y. Qiu, J. Li and Z. Wang, *Int. J. Food Microbiol.*, 2017, **261**, 42–48.
17 Y. Zhao, Y. Ma, R. Zhou, Y. He, Y. Wu, Y. Yi and G. Zhu, *J. Food Meas. Char.*, 2022, **16**, 2596–2603.
18 J. Wang, Y.-q. Chen, Y.-j. Liu, G.-k. Liu, R.-j. Cai and J. Wang, *Appl. Therm. Eng.*, 2023, **219**, 119602.
19 L. Wang, B. B. Xin, A. Elsukova, P. Eklund and N. Solin, *ACS Sustain. Chem. Eng.*, 2020, **8**, 17368–17378.
20 Y. Wang, S. Wu, Q. Yin, K. Du, Q. Yin, B. Jiang and S. Mo, *ACS Appl. Mater. Interfaces*, 2021, **13**, 23970–23982.
21 W. Xue, G. Zhang, L. Chen and K. Li, *J. Build. Eng.*, 2024, **84**, 108561.
22 T. J. Zhu, *J. Inorg. Mater.*, 2019, **34**, 233–235.
23 W. Zhang, L. Li, S. Li, J. Ma, C. Liu and Y. Bao, *Acta Mater. Compos. Sin.*, 2022, **39**, 3104–3120.
24 Y. Qin, Y. Zeng, D. Wang, Y. Yang and X. Lu, *Acta Mater. Compos. Sin.*, 2022, **39**, 3330–3338.
25 L. Li, W.-D. Liu, Q. Liu and Z.-G. Chen, *Adv. Funct. Mater.*, 2022, **32**, 2200548.
26 P.-a. Zong, J. Liang, P. Zhang, C. Wan, Y. Wang and K. Koumoto, *ACS Appl. Energy Mater.*, 2020, **3**, 2224–2239.
27 W. Zeng, X.-M. Tao, S. Lin, C. Lee, D. Shi, K.-h. Lam, B. Huang, Q. Wang and Y. Zhao, *Nano Energy*, 2018, **54**, 163–174.
28 W. Kong, H. Kum, S.-H. Bae, J. Shim, H. Kim, L. Kong, Y. Meng, K. Wang, C. Kim and J. Kim, *Nat. Nanotechnol.*, 2019, **14**, 927–938.
29 F. Zhang, K. Yang, G. Liu, Y. Chen, M. Wang, S. Li and R. Li, *Composites, Part A*, 2022, **160**, 107051.
30 S. H. Zaferani, R. Ghomashchi and D. Vashaee, *ACS Appl. Energy Mater.*, 2021, **4**, 3573–3583.
31 H. Terrones, R. Lv, M. Terrones and M. S. Dresselhaus, *Rep. Prog. Phys.*, 2012, **75**, 062501.
32 C. Li, Z. Zhou, Y. Lou and L. Fu, *Microstructures*, 2025, **5**, 2025075.
33 X. Qian, J. Zhou and G. Chen, *Nat. Mater.*, 2021, **20**, 1188–1202.
34 S. Rafique, M. R. Burton, N. Badiei, J. Gonzalez-Feijoo, S. Mehraban, M. J. Carnie, A. Tarat and L. Li, *ACS Appl. Mater. Interfaces*, 2020, **12**, 30643–30651.
35 D. Zhang, Y. Mao, P. Bai, Q. Li, W. He, H. Cui, F. Ye, C. Li, R. Ma and Y. Chen, *Nano Lett.*, 2022, **22**, 3417–3424.
36 D. C. Marcano, D. V. Kosynkin, J. M. Berlin, A. Sinitskii, Z. Z. Sun, A. Slesarev, L. B. Alemany, W. Lu and J. M. Tour, *ACS Nano*, 2010, **4**, 4806–4814.
37 S. Eigler and A. Hirsch, *Angew. Chem., Int. Ed.*, 2014, **53**, 7720–7738.
38 K. Parvez, Z. S. Wu, R. J. Li, X. J. Liu, R. Graf, X. L. Feng and K. Müllen, *J. Am. Chem. Soc.*, 2014, **136**, 6083–6091.
39 H. Bark, M. Ko, M. Lee, W. Lee, B. Hong and H. Lee, *ACS Sustain. Chem. Eng.*, 2018, **6**, 7468–7474.
40 P. Tian, L. Tang, K. S. Teng, J. Xiang and S. P. Lau, *Adv. Mater. Technol.*, 2019, **4**, 1900007.
41 A. Samal, C. Mohanty, N. Das, R. Das and M. F. Kühnel, *Mater. Today Chem.*, 2024, **38**, 102096.
42 S. Yang, P. Qiu, L. Chen and X. Shi, *Small Sci.*, 2021, **1**, 2100005.
43 H. J. Hwang, S.-Y. Kim, S. K. Lee and B. H. Lee, *Carbon*, 2023, **201**, 467–472.
44 J. Liu, G. Liu, J. Xu, C. Liu, W. Zhou, P. Liu, G. Nie, X. Duan and F. Jiang, *ACS Appl. Energy Mater.*, 2020, **3**, 6165–6171.
45 T. G. Novak, J. Kim, J. Kim, A. P. Tiwari, H. Shin, J. Y. Song and S. Jeon, *Adv. Funct. Mater.*, 2020, **30**, 2001760.
46 Y. Zhang, L. Zhang and C. Zhou, *Acc. Chem. Res.*, 2013, **46**, 2329–2339.
47 B. Deng, Z. Liu and H. Peng, *Adv. Mater.*, 2019, **31**, 1800996.
48 K. Chen, L. Shi, Y. Zhang and Z. Liu, *Chem. Soc. Rev.*, 2018, **47**, 3018–3036.
49 M. Schrade, W. Xing, K. Thorshaug and B. D. Belle, *ACS Appl. Electron. Mater.*, 2022, **4**, 1506–1510.
50 M. Choi, T. G. Novak, J. Byen, H. Lee, J. Baek, S. Hong, K. Kim, J. Song, H. Shin and S. Jeon, *ACS Appl. Mater. Interfaces*, 2021, **13**, 24304–24313.
51 Y. Wu, J. Zhu and L. Huang, *Carbon*, 2019, **143**, 610–640.
52 V. K. R. Kondapalli, O. I. Akinboye, Y. Zhang, G. Donadey, J. Morrow, K. Brittingham, A. A. Raut, M. Khosravifar, B. Al-Riyami, J.-H. Bahk and V. Shanov, *ACS Appl. Mater. Interfaces*, 2024, **16**, 13150–13160.
53 F. Liu, Y. Sun, Z. Li, P. Peng, C. Wang and H. Wang, *Microstructures*, 2025, **5**, 2025043.

 © 2025 The Author(s). Published by the Royal Society of Chemistry

Open Access Article. Published on 28 July 2025. Downloaded on 12/27/2025 3:34:44 PM. This article is licensed under a Creative Commons Attribution-NonCommercial 3.0 Unported Licence.

54 Y. Chao, J. Pang, Y. Bai, P. Wu, J. Luo, J. He, Y. Jin, X. Li, J. Xiong, H. Li and W. Zhu, *Food Chem.*, 2020, **320**, 126666.
55 I. T. Witting, T. C. Chasapis, F. Ricci, M. Peters, N. A. Heinz, G. Hautier and G. J. Snyder, *Adv. Electron. Mater.*, 2019, **5**, 1800904.
56 M. M. Rashad, A. El-Dissouky, H. M. Soliman, A. M. Elseman, H. M. Refaat and A. Ebrahim, *Mater. Res. Innovations*, 2018, **22**, 315–323.
57 H. Wei, PhD thesis, The Chinese University of Hong Kong, Hong Kong, 2020.
58 T. Cao, X.-L. Shi, M. Li, B. Hu, W. Chen, W.-D. Liu, W. Lyu, J. MacLeod and Z.-G. Chen, *eScience*, 2023, **3**, 100122.
59 K. Ahmad, C. Wan, M. A. Al-Eshaikh and A. N. Kadachi, *Appl. Surf. Sci.*, 2019, **474**, 2–8.
60 S. Li, T. Fan, X. Liu, F. Liu, H. Meng, Y. Liu and F. Pan, *ACS Appl. Mater. Interfaces*, 2017, **9**, 3677–3685.
61 A. Nour, H. M. Refaat, A. El-Dissouky and H. M. Soliman, *Ceram. Int.*, 2023, **49**, 26982–26993.
62 K. Ahmad, C. Wan, M. Al-Eshaikh and A. Kadachi, *Appl. Surf. Sci.*, 2019, **474**, 2–8.
63 J. Bae, S. Jo, S.-h. Jung, J. M. Park, C. M. Kim, K.-I. Park and K. T. Kim, *ACS Appl. Mater. Interfaces*, 2024, **16**, 47844–47853.
64 Z. Zhang, K. Zhao, T.-R. Wei, P. Qiu, L. Chen and X. Shi, *Energy Environ. Sci.*, 2020, **13**, 3307–3329.
65 B. Q. He, K. Zhang and M. Y. Zhu, *Green Energy Environ.*, 2025, **10**, 619–688.
66 W. D. Liu, L. Yang, Z. G. Chen and J. Zou, *Adv. Mater.*, 2020, **32**, 1905703.
67 M. Li, D. L. Cortie, J. Liu, D. Yu, S. M. K. N. Islam, L. Zhao, D. R. G. Mitchell, R. A. Mole, M. B. Cortie, S. Dou and X. Wang, *Nano Energy*, 2018, **53**, 993–1002.
68 Q. Yan and M. G. Kanatzidis, *Nat. Mater.*, 2022, **21**, 503–513.
69 D. Yang, H. Bai, X. Su, Z. Li, T. Luo, J. Li, H. Tang, H. Luo, Q. Zhang and C. Uher, *Cell Rep. Phys. Sci.*, 2021, **2**, 100345.
70 K. Zhao, E. Eikeland, D. He, W. Qiu, Z. Jin, Q. Song, T.-r. Wei, P. Qiu, J. Liu and J. He, *Joule*, 2021, **5**, 1183–1195.
71 Z. Zhou, Y. Huang, B. Wei, Y. Yang, D. Yu, Y. Zheng, D. He, W. Zhang, M. Zou, J.-L. Lan, J. He, C.-W. Nan and Y.-H. Lin, *Nat. Commun.*, 2023, **14**, 2410.
72 O. Caballero-Calero, J. R. Ares and M. Martín-González, *Adv. Sustainable Syst.*, 2021, **5**, 2100095.
73 L. Chen, Z. Liu, Z. Guo and X.-J. Huang, *J. Mater. Chem. A*, 2020, **8**, 17326–17359.
74 S. Sakthivel, S. Shobika, A. Dinesh, K. Yogalakshmi, R. Suriyaprakash, B. Kabilan, P. Sathyajith, S. Elumalai, L. Gnanasekaran and M. Ayyar, *Results Chem.*, 2025, **13**, 101956.
75 G. Sanyal, B. Mondal, C. S. Rout and B. Chakraborty, *Energy Storage*, 2023, **5**, e432.
76 M. A. Jenisha, S. Kavirajan, S. Harish, J. Archana, K. Kamalabharathi, E. S. Kumar and M. Navaneethan, *J. Alloys Compd.*, 2022, **895**, 162493.
77 K. Aishwarya, R. Rajavardhini, S. Maruthasalamoorthy, J. Mani, R. Nirmala, G. Anbalagan and N. Rangaswamy, *ACS Appl. Nano Mater.*, 2024, **7**, 23568–23579.
78 B. L. Phoon, C. W. Lai, J. C. Juan, P. L. Show and W. H. Chen, *Int. J. Energy Res.*, 2019, **43**, 5151–5174.
79 Y. Zhu, J. M. Skelton, D. J. Lewis and R. Freer, *J. Phys.: Energy*, 2024, **6**, 025027.
80 X. Li, X. Luo, M. Wang, T. Lyu, C. Zhang, F. Liu, H. Ma and L. Hu, *Microstructures*, 2025, **5**, 2025008.
81 Y. Lin, C. Norman, D. Srivastava, F. Azough, L. Wang, M. Robbins, K. Simpson, R. Freer and I. A. Kinloch, *ACS Appl. Mater. Interfaces*, 2015, **7**, 15898–15908.
82 D. Ekren, J. Cao, F. Azough, D. Kepaptsoglou, Q. Ramasse, I. A. Kinloch and R. Freer, *ACS Appl. Mater. Interfaces*, 2022, **14**, 53711–53723.
83 A. G. H. Smith, PhD thesis, UCL (University College London), 2012.
84 S. S. Jana, D. Chatterjee and T. Maiti, *ACS Appl. Mater. Interfaces*, 2023, **15**, 48246–48254.
85 D. Ekren, F. Azough and R. Freer, in *Thermoelectric Energy Conversion: Theories and Mechanisms, Materials, Devices, and Applications*, Woodhead Publishing, Woodhead, 2021, pp. 303–311.
86 T. R. Bhandari, R. P. Bhattarai and R. Adhikari, *J. Mater. Sci.*, 2024, **59**, 1–17.
87 N. Davis, A. R, S. Muraleedharan, V. Thiruvenkatam, J. Mayandi, T. G. Finstad, I. Razanau, U. Novikau and A. M. Ashok, *Ceram. Int.*, 2022, **48**, 24454–24461.
88 D. Chen, Y. Zhao, Y. Chen, B. Wang, H. Chen, J. Zhou and Z. Liang, *ACS Appl. Mater. Interfaces*, 2015, **7**, 3224–3230.
89 Y. Cui and Y. Wei, *Cem. Concr. Compos.*, 2022, **128**, 104442.
90 R. S. Sankar, S. Anwar and S. Anwar, *Phys. B*, 2023, **652**, 414620.
91 A. Nozariasbmarz, F. Suarez, J. H. Dycus, M. J. Cabral, J. M. LeBeau, M. C. Öztürk and D. Vashaee, *Nano Energy*, 2020, **67**, 104265.
92 H. Jin, J. Li, J. Iocozzia, X. Zeng, P. C. Wei, C. Yang, N. Li, Z. Liu, J. H. He and T. Zhu, *Angew. Chem., Int. Ed.*, 2019, **58**, 15206–15226.
93 E. Muchuweni and E. T. Mombeshora, *Renew. Energy Focus*, 2023, **45**, 40–52.
94 Y. Yang, H. Deng and Q. Fu, *Mater. Chem. Front.*, 2020, **4**, 3130–3152.
95 E. Dauzon, X. Sallenave, C. Plesse, F. Goubard, A. Amassian and T. D. Anthopoulos, *Adv. Mater.*, 2021, **33**, 2101469.
96 M. Y. Zhu, B. Q. He, K. Zhang, S. Hussain and T. Li, *Mater. Chem. Front.*, 2024, **8**, 2454–2492.
97 M. Hassan, G. Abbas, N. Li, A. Afzal, Z. Haider, S. Ahmed, X. Xu, C. Pan and Z. Peng, *Adv. Mater. Technol.*, 2022, **7**, 2100773.
98 L. Zhang, W. Du, A. Nautiyal, Z. Liu and X. Zhang, *Sci. China Mater.*, 2018, **61**, 303–352.
99 H. Lee, K. Paeng and I. S. Kim, *Synth. Met.*, 2018, **244**, 36–47.
100 K. Xu, G. Chen and D. Qiu, *J. Mater. Chem. A*, 2013, **1**, 12395–12399.
101 T. Li, A. D. Pickel, Y. Yao, Y. Chen, Y. Zeng, S. D. Lacey, Y. Li, Y. Wang, J. Dai and Y. Wang, *Nat. Energy*, 2018, **3**, 148–156.
102 J. Xiong, F. Jiang, H. Shi, J. Xu, C. Liu, W. Zhou, Q. Jiang, Z. Zhu and Y. Hu, *ACS Appl. Mater. Interfaces*, 2015, **7**, 14917–14925.

Open Access Article. Published on 28 July 2025. Downloaded on 12/27/2025 3:34:44 PM.
This article is licensed under a Creative Commons Attribution-NonCommercial 3.0 Unported Licence.

103 M. R. Shankar and A. Prabhu, *J. Mater. Sci.*, 2023, **58**, 16591–16633.
104 Y. Wang, H. Pang, Q. Guo, N. Tsujii, T. Baba, T. Baba and T. Mori, *ACS Appl. Mater. Interfaces*, 2021, **13**, 51245–51254.
105 A. H. Majeed, L. A. Mohammed, O. G. Hammoodi, S. Sehgal, M. A. Alheety, K. K. Saxena, S. A. Dadoosh, I. K. Mohammed, M. M. Jasim and N. U. Salmaan, *Int. J. Polym. Sci.*, 2022, **2022**, 9047554.
106 Sonika, S. K. Verma, S. Samanta, A. K. Srivastava, S. Biswas, R. M. Alsharabi and S. Rajput, *Adv. Mater. Sci. Eng.*, 2022, **2022**, 2266899.
107 C. Zhan, G. Yu, Y. Lu, L. Wang, E. Wujcik and S. Wei, *J. Mater. Chem. C*, 2017, **5**, 1569–1585.
108 X.-L. Shi, L. Wang, W. Lyu, T. Cao, W. Chen, B. Hu and Z.-G. Chen, *Chem. Soc. Rev.*, 2024, **53**, 9254–9305.
109 L. Wang, H. Bi, Q. Yao, D. Ren, S. Qu, F. Huang and L. Chen, *Compos. Sci. Technol.*, 2017, **150**, 135–140.
110 N. D. Wood, J. S. Tse, J. M. Skelton, D. J. Cooke, L. J. Gillie, S. C. Parker and M. Molinari, *J. Mater. Sci. Technol.*, 2023, **166**, 250–260.
111 Y.-H. Lin, T.-C. Lee, Y.-S. Hsiao, W.-K. Lin, W.-T. Whang and C.-H. Chen, *ACS Appl. Mater. Interfaces*, 2018, **10**, 4946–4952.
112 A. C. S. Costa, C. A. Furtado and R. L. Oréfice, *J. Appl. Polym. Sci.*, 2023, **141**, 12395–12399.
113 M. K. Ali, A. Hessein, M. A. Hassan, M. Ghali, N. M. Shaalan, K. Nakamura and A. A. El-Moneim, *J. Appl. Polym. Sci.*, 2021, **138**, 50852.
114 A. Panbude, S. Sathiyamoorthy, R. Kumar, H. Shankar, S. Paulraj, V. Kathirvel, A. M. Adam, E. M. M. Ibrahim, K. Jayabal and P. Veluswamy, *Mater. Lett.*, 2021, **304**, 130576.
115 S. M. Hus and A.-P. Li, *Prog. Surf. Sci.*, 2017, **92**, 176–201.
116 S. Dey, in *Functional Properties of Advanced Engineering Materials and Biomolecules*, Springer, Berlin, 2021, pp. 201–235.
117 M. Xu, T. Liang, M. Shi and H. Chen, *Chem. Rev.*, 2013, **113**, 3766–3798.
118 A. Giri, S. G. Walton, J. Tomko, N. Bhatt, M. J. Johnson, D. R. Boris, G. Lu, J. D. Caldwell, O. V. Prezhdo and P. E. Hopkins, *ACS Nano*, 2023, **17**, 14253–14282.
119 M. S. Zoromba, M. Abdel-Aziz, M. Bassyouni, A. M. Abusorrah, A. Attar, N. Baghdadi and N. Salah, *Phys. E*, 2021, **134**, 114889.
120 S. Wang, F. Liu, C. Gao, T. Wan, L. Wang, L. Wang and L. Wang, *Chem. Eng. J.*, 2019, **370**, 322–329.
121 J. Chen, J. Liu, T. Thundat and H. Zeng, *ACS Appl. Mater. Interfaces*, 2019, **11**, 18720–18729.
122 Y. Liu and F. Wu, *Nanoscale Adv.*, 2023, **5**, 3606–3618.
123 Y. Du, H. Niu, J. Li, Y. Dou, S. Z. Shen, R. Jia and J. Xu, *Polymers*, 2018, **10**, 1143.
124 A. Debnath, K. Deb, K. L. Bhowmik and B. Saha, *ACS Appl. Energy Mater.*, 2020, **3**, 7772–7781.
125 S. Han, W. Zhai, G. Chen and X. Wang, *RSC Adv.*, 2014, **4**, 29281–29285.
126 Y. Wang, J. Yang, L. Wang, K. Du, Q. Yin and Q. Yin, *ACS Appl. Mater. Interfaces*, 2017, **9**, 20124–20131.
127 S. Yang, Y. Jiang, S. Li and W. Liu, *Carbon*, 2017, **111**, 513–518.
128 S. Feng, N. Luo, A. Tang, W. Chen, Y. Zhang, S. Huang and W. Dou, *J. Phys. Chem. C*, 2019, **123**, 16614–16620.
129 C. Yao, C. Kong, H.-F. Feng, Y. Dong, L. Huang, X. Zhang, Z. Song and Z.-X. Guo, *J. Phys. Chem. C*, 2024, **129**, 52–60.
130 R. Batra, L. Song and R. Ramprasad, *Nat. Rev. Mater.*, 2021, **6**, 655–678.
131 K. Guo, Z. Yang, C.-H. Yu and M. J. Buehler, *Mater. Horiz.*, 2021, **8**, 1153–1172.
132 J. Deng, M. Li and Y. Wang, *Green Chem.*, 2016, **18**, 4824–4854.
133 P. Yu, S. E. Lowe, G. P. Simon and Y. L. Zhong, *Curr. Opin. Colloid Interface Sci.*, 2015, **20**, 329–338.
134 C.-Y. Su, A.-Y. Lu, Y. Xu, F.-R. Chen, A. N. Khlobystov and L.-J. Li, *ACS Nano*, 2011, **5**, 2332–2339.
135 F. Liu, C. Wang, X. Sui, M. A. Riaz, M. Xu, L. Wei and Y. Chen, *Carbon Energy*, 2019, **1**, 173–199.

 © 2025 The Author(s). Published by the Royal Society of Chemistry